doi:10.26443/seismica.v4i2.1696

# A River on Fiber: High Resolution Fluvial Monitoring with Distributed Acoustic Sensing

**Danica L. Roth** [*1], **Maximiliano J. Bezada** [2], **Ge Jin** [3], **Claire C. Masteller** [4], **Matthew R. Siegfried** [3,5], **Aleksei Titov** [3], **Bill Tate**[2]

[1]Cooperative Institute for Research In Environmental Sciences, University of Colorado, Boulder, CO, USA., [2]Earth & Environmental Sciences, University of Minnesota, Minneapolis, MN, USA., [3]Department of Geophysics, Colorado School of Mines, Golden, CO, USA., [4]Earth, Environmental, and Planetary Sciences, Washington University in St. Louis, St. Louis, MO, USA., [5]Hydrologic Science & Engineering Program, Colorado School of Mines, Golden, CO, USA.

Author contributions: *Conceptualization*: D. Roth, G. Jin, M. Siegfried, C. Masteller. *Data Curation*: G. Jin, A. Titov. *Formal Analysis*: D. Roth, M. Bezada, B. Tate. *Funding Acquisition*: G. Jin, M. Siegfried, D. Roth, M. Bezada. *Investigation*: D. Roth, G. Jin, M. Siegfried, A. Titov. *Methodology*: D. Roth, M. Bezada, G. Jin. *Project Administration*: D. Roth, M. Bezada. *Resources*: G. Jin, M. Siegfried, D. Roth. *Software*: D. Roth, M. Bezada, G. Jin, A. Titov, B. Tate. *Supervision*: D. Roth, M. Bezada, G. Jin. *Validation*: G. Jin, D. Roth. *Visualization*: D. Roth, M. Bezada. *Writing – original draft*: D. Roth, M. Bezada, C. Masteller. *Writing – review & editing*: D. Roth, M. Bezada, G. Jin, M. Siegfried, C. Masteller.

**Abstract** Fluvially generated seismo-acoustic waves offer a novel means of investigating river processes, yet interpreting signals from individual seismometers or hydrophones remains challenging. This study demonstrates the potential of distributed acoustic sensing (DAS) for fluvial monitoring. We present strain-rate measurements and power spectra recorded at sub-meter resolution along ~160 m of submerged fiber-optic cable in Clear Creek, CO, USA. We find that regions of enhanced turbulence, such as rapids, are associated with broadband signals, whereas reaches with less turbulent flow display spectral power within distinct frequency bands. In three such regions, we observe harmonic frequency banding with pronounced spatio-spectral gliding (i.e., peak frequencies vary systematically along-river). One of these regions is colocated with the source of a recurring impulsive signal characterized by audible "knocking" sounds in the acoustic strain-rate data. We use travel time analysis to determine that this signal is generated by cable-bed impacts due to turbulence-driven cable oscillation. Model results further indicate that along-cable variation in the lags between pulses and their reflections produces the banded spatio-spectral gliding. Our observations highlight the capacity for array methods to interrogate distinct signal sources in DAS data and emphasize the need for improved deployment techniques in dynamic fluvial environments.

Production Editor:
Yen Joe Tan
Handling Editor:
Wenbo Wu
Copy & Layout Editor:
Oliver Lamb

Signed reviewer(s):
Ron Nativ

Received:
April 14, 2025
Accepted:
October 20, 2025
Published:
November 17, 2025

**Non-technical summary** Monitoring or predicting the movement of water and sediment in rivers is an important challenge in many fields. Sound waves produced by rivers offer a new way of "seeing" beneath the water's surface, but individual recordings are difficult to interpret because river environments are very complex. We use distributed acoustic sensing (DAS), a method for measuring acoustic signals with a fiber optic cable, to collect the first record of sound waves and turbulent motion along a fiber optic cable submerged in a river. This record provides a high-resolution snapshot of sound and motion from each point along a ~160 m stretch of Clear Creek in Colorado, USA, allowing us to identify the signatures of river features like pools and rapids, and to examine how acoustic frequency or pitch changes along-stream. The detail in the DAS recordings confirms that acoustic waves contain valuable information about the riverbed and flow and allows us to locate the sources of specific signals, including some generated by movement of the cable itself. This study shows that DAS technology can dramatically improve our ability to monitor rivers with sound waves and also highlights some of the challenges that future work should address in the development of this tool.

## 1 Introduction

Passive seismo-acoustic techniques are increasingly used to study surface processes and Earth materials that generate or modify elastic waves (Malehmir et al., 2016; Jerolmack and Daniels, 2019; Piégay et al., 2020; Cook and Dietze, 2022). In rivers, both in-stream (e.g., Geay et al., 2020) and along-bank (e.g., Burtin et al., 2016) seismo-acoustic instrumentation show great promise for continuous detection and monitoring of sediment transport and fluid hydrodynamics, which are challenging to observe through other methods.

In-stream hydrophones and geophones record fluvial soundscapes over frequencies from Hz to tens of kHz (e.g., Wyss et al., 2016; Geay et al., 2017) and have been used to inform studies of fish habitat (e.g., Tonolla et al., 2011), sediment transport (e.g., Krein et al., 2007; Rickenmann, 2017; Petrut et al., 2018), and hydrometry (e.g., Osborne et al., 2021). Alternatively, seismometers and geophones deployed outside the stream channel integrate diverse fluvial signals and attenuation effects over broader spatial scales (e.g., Larose et al., 2015). Continuous archival seismic data have revealed

*Corresponding author: danica.roth@colorado.edu

new connections to environmental forcings (e.g., Chao et al., 2015; Cook et al., 2018), and targeted deployments have provided constraints on sediment transport (e.g., Schmandt et al., 2013, 2017; Misset et al., 2020) and fluid hydrodynamics (e.g., Goodling et al., 2018).

Despite both theoretical and empirical advances connecting seismo-acoustic signals to specific processes, robust and quantitative interpretation of signals in real settings remains a major challenge that limits the utility of in-stream and bankside monitoring efforts alike (e.g., Roth et al., 2017). In-stream hydrophones can capture the high-frequency signals generated by both water turbulence and sediment transport, and in some cases these processes have been associated with distinct frequency bands in the tens of Hz to tens of kHz range (e.g., Thorne and Hanes, 2002; Belleudy et al., 2010; Krein et al., 2016). However, because acoustic amplitudes attenuate rapidly at these high frequencies, hydroacoustic wave fields are highly sensitive to the distance from a signal source and the local hydraulic conditions controlling turbulence intensity. As a result, quantitative analysis of hydrophone records requires site-specific calibration (e.g., Tonolla et al., 2010, 2011) and cannot differentiate between the effects of signal source proximity and strength. Quantifying bedload flux therefore requires independent methods of constraining the signal source location (Geay et al., 2017) and attenuation (Geay et al., 2019). In-stream instruments can also be expensive and logistically challenging to install, are at risk of damage or loss at high flows, and can produce turbulent noise due to the footprint of instruments and mounting infrastructure in the flow (e.g., Belleudy et al., 2010).

Seismic deployments outside the flow can avoid these issues, but face their own challenges due to the lack of constraints on a wider range of source signals combined with near-field attenuation through heterogeneous fluvial substrates (e.g., Roth et al., 2017). Theoretical models (Tsai et al., 2012) and observations from alluvial channels (e.g., Roth et al., 2016) indicate nearly complete attenuation of river-generated seismic power above ~100–200 Hz over 1s to 10s of meters. The high-frequency signals that are lost before reaching along-bank seismometers contain valuable information detectable on hydrophones, for example, about bedload particle sizes (e.g., Belleudy et al., 2010). Theoretical seismic models for sediment transport (Tsai et al., 2012) and turbulence (Gimbert et al., 2014) show promise but remain largely unvalidated in real settings due to reliance on model parameters requiring site-specific calibration (Dietze et al., 2018).

Distributed acoustic sensing (DAS) may provide a practical approach to overcoming to these logistical and scientific challenges. DAS systems inject laser pulses into fiber optic cables and use optical phase shifts and return times of back-scattered light to measure along-fiber distributed dynamic strain rates (Lindsey and Martin, 2021). DAS records are comparable to large-N geophone arrays, but offer unprecedented spatial and temporal resolution: cables can be tens of kilometers long with spatial resolution of meters and can resolve frequencies from millihertz to kilohertz. Power and data logging are centralized through a single interrogator unit, reducing field logistics and pre-processing relative to multi-node arrays. Rugged military-grade fiber optic cables make DAS more straightforward to deploy both in-stream and along-bank relative to geophone arrays with comparable spatial resolution and coverage. With typical diameters of < 1 cm, DAS cables will also produce a narrower physical footprint in the flow than hydrophones (~1-10 cm diameters), which may lead to less self-generated noise due to wake turbulence. Growing use of DAS in environmental fields has yielded recent insights on topics including slope failure (Michlmayr et al., 2016), groundwater dynamics (Ajo-Franklin et al., 2019; Gao et al., 2020; Rodríguez Tribaldos and Ajo-Franklin, 2021), hydrofracturing (Becker et al., 2020), shallow seismic velocities (Yang et al., 2022), glacial icequakes (Walter et al., 2020), glacial crystal fabric and subglacial sediment properties (Booth et al., 2020), ocean flow dynamics and subsurface structure (Lindsey et al., 2019; Cheng et al., 2021) and the songs of baleen whales (Bouffaut et al., 2022). In fluvial systems, DAS offers to merge the unique advantages of high frequency in-stream hydrophone monitoring with the broad spatial extent and array-based methodologies of seismic and geophone deployments. To date, however, this potential has not been explored.

Here, we present results from the first in-stream DAS deployment in Clear Creek, CO, USA as proof of concept for the utilization of DAS to monitor and study fluvial processes. In this contribution, our objectives are to: 1) demonstrate that high-resolution hydroacoustic data collected by DAS arrays has the potential to provide useful information about fluvial processes such as flow hydraulics and bedload; 2) discuss our observations and the advantages and limitations of DAS relative to previous work with more established hydroacoustic monitoring tools, namely hydrophones and seismometers; and 3) identify opportunities, needs and challenges relevant to future DAS deployments in fluvial environments.

Our results show that meter-resolution DAS data allow clear discrimination of river morphology associated with strain rate and spectral features generated by both acoustic waves and direct interaction between the cable and flow. These features are broadly consistent with previous, lower resolution seismic and hydroacoustic observations (e.g., Tonolla et al., 2009, 2010, 2011) that validate their reliability, but provide an additional level of detail due to the spatial resolution of measurements along the DAS cable. We document a recurring pulse signal analogous to bedload impacts, and use array methods to locate and identify its source as interactions between the cable and bed rather than sediment transport. In addition to cable-bed interaction, we also identify turbulence-induced cable motion and along-cable wave transmission. The high frequency and spatial density of the DAS data further enables detection of spatio-spectral gliding or systematic variation in peak frequencies along the river. We show that this phenomenon likely results from distance-dependent lags between pulse signals and their reflections, and discuss other hypothetical mechanisms that might lead to spectral gliding in fluvial settings. Finally, we discuss opportunities for future deployments and challenges that

must be addressed to enable quantitative interpretation of fluvial DAS data.

## 2 Study Site

Clear Creek is located in Golden, CO, USA (Figure 1a), with mean annual discharge of 5.4 $m^3/s$ and peak flows (~35 $m^3/s$) fed by seasonal snowmelt, with storm-flow in summer. Within the ~160 m alluvial test section, the bankfull channel width is ~27 m and the mean channel bed gradient is ~0.003. Within the study reach, the stream transitions from a pool-riffle or run-riffle morphology upstream to an engineered step-pool morphology with cement-reinforced rapids (used as a recreational waterpark during high flow) and deeper gravel- and cobble-bedded pools downstream (Figure 1a). Aside from the cemented rapids, the bed is a coarse, cobbly gravel deposit of mixed sedimentary and granitic or gneissic crystalline material with median grain diameter $D_{50}$ ~ 0.05 m, generally less than 6 m thick (Trimble and Machette, 2003) and overlying shale and sandstone bedrock (Van Horn, 1972).

## 3 Methods

### 3.1 DAS deployment and geospatial referencing

On December 6, 2020, we deployed a Terra15 Treble DAS system with a military grade fiber optic cable rated for rugged outdoor deployments. Optical phase shift data were collected at 20,737 Hz at discrete points (known as "channels") every 0.82 m along the cable for ~15 minutes. The cable, ~7 mm in diameter and housing two single-mode optical fibers in polyurethane, was placed in three roughly parallel folds: submerged along the creek, immediately adjacent to the flow along a gravel point bar and engineered bank slope within the bankfull stream channel, and along the floodplain above the active stream bed (Figure 1a). Due to the bank geometry and prevalence of cement and boulders, coupling between the along-bank cable segment and the ground was inconsistent, with some sections of cable suspended in the air or partially submerged along the edges of pools (Figure 1a-b). We therefore present data only from the submerged cable segment.

The upstream end of the submerged cable segment was anchored around a tree stump on the bank. Because cable burial within the bed was impossible through the cement-bedded engineered rapids, the submerged cable length was deployed along the stream thalweg, or the path of deepest flow, with the downstream end unanchored. We allowed the cable to self-adjust under flow-induced tension before commencing data collection. This method ensured maximum stability of the tensioned cable position despite drag from the flow. At the upstream end of the study reach, just downstream of the stump anchor, ~10 m of cable was suspended under tension before entering the flow.

To map along-cable distances to georeferenced positions on the creek, we conducted "tap tests" at 17 points outside the flow, tugging the cable in opposing directions to produce a sharply polarized (positive/negative), high-amplitude strain signal in the closest DAS channels on either side of the tap test location. Tap tests were documented with time- and Global Positioning System (GPS)-tagged photographs. The closest DAS channel to each tap test was then identified by finding the polarized signal in the downsampled, 0.1–1 Hz bandpassed DAS data. Uncertainty in the along-cable tap-test locations is therefore a maximum of 0.82 m, or the distance between DAS channels.

We used deployment photographs (e.g., Figure 1b and Supplemental Figure S1) and satellite imagery (Google Earth Pro, 2019) cross-validated with a 1 m resolution lidar-derived digital surface model (U.S. Geological Survey, 2015) to manually validate the tap test GPS locations and reconstruct the cable path in Google Earth Pro (Figure 1a). Estimated confidence in the corrected tap test GPS locations is ±1 m. Final cumulative distances measured along the reconstructed cable path fall within 2.45 m of the known along-cable distances for all identified tap test locations.

The tap test conducted closest to the submerged section of cable, ~1 m away from the flow, was not detectable against background flow-generated noise, and tap tests were therefore not conducted along the submerged section of cable. Cable positioning within the flow was constrained through field observations, photographs, and satellite imagery. Where the cable position could not be verified by photographs or observations, we estimated its position based on the constraints of channel geometry and the fact that the cable was under tension by the flow. Cable positioning was further cross-validated using the known along-cable distance between the last georeferenced tap test position at the upstream end of the study reach and the distal end of the cable, which was observed to reach the far edge of the third rapid downstream. Given these constraints, we conservatively estimate the spatial accuracy of signals we present here to be within ~5 m in the along-stream direction. Where visible throughout the deployment, the tensioned cable demonstrated no detectable lateral or vertical translation. At the far downstream end, the free-floating cable tail exhibited noticeable oscillatory motion attributed to water turbulence downstream of the third engineered rapid. Data from this section of cable is excluded from our analysis.

### 3.2 Conditions during deployment

During the ~15-minute deployment, mean discharge was ~1.2 $m^3/s$ (USGS stream gage 06719505, ~350 m upstream; U.S. Geological Survey, 2016). Flow depth and depth-averaged velocity were measured manually at several representative points along the thalweg using a Hach FH950 Flowmeter at 60% relative depth (i.e., 60% of the total depth measured from the surface of the water). Active channel (i.e., flow) width at each location was measured manually with tape measures. Representative thalweg depths for rapids, riffle, and pools respectively were 0.21, 0.43, and 0.55 m, with associated velocities of 1.26, 0.77, and 0.24 m/s, and active

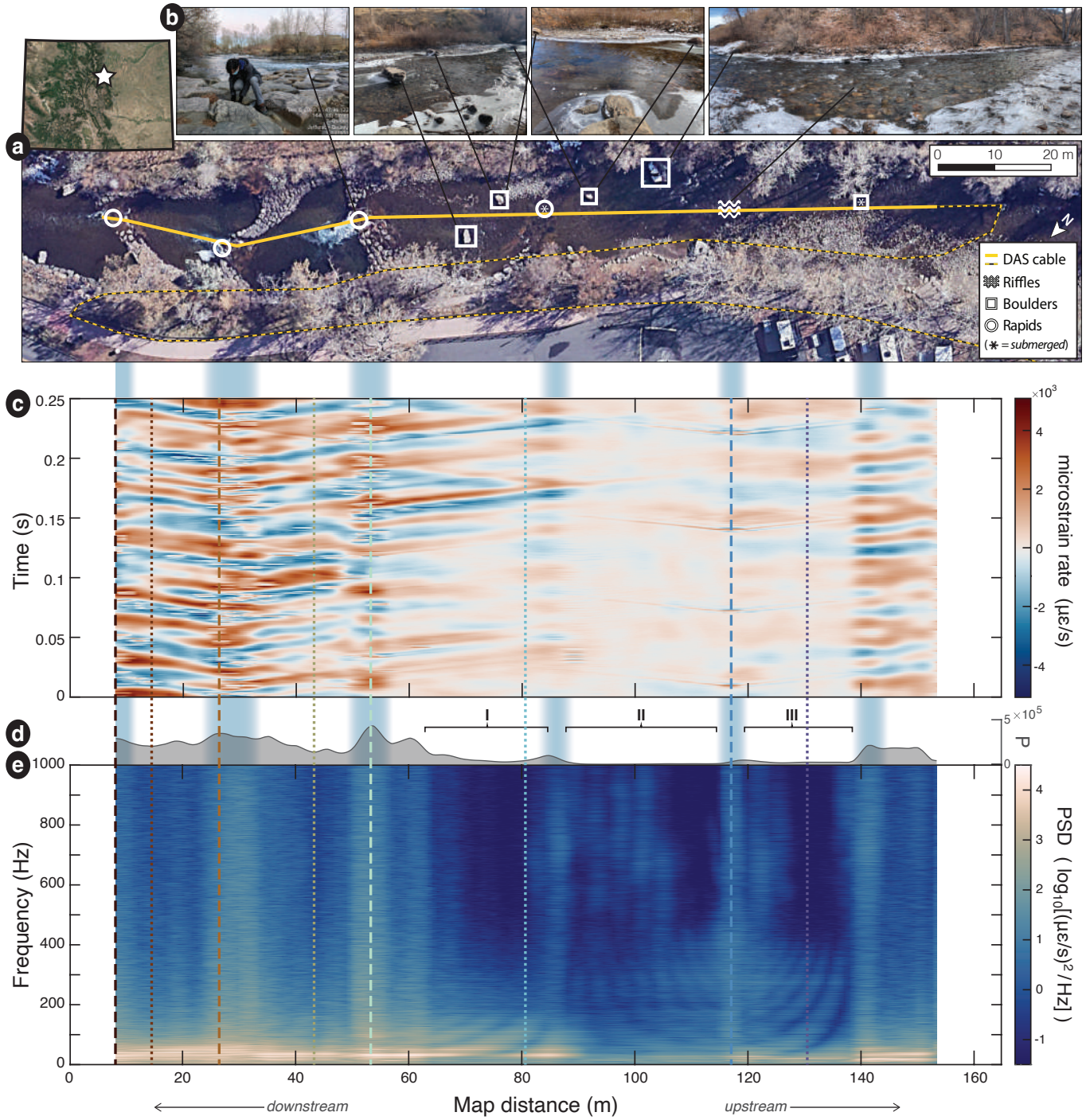


**Figure 1** Spatially aligned field site, microstrain rate, and power spectral density maps with reference imagery. **a)** Study location in Colorado and site map (downstream end of study reach at map distance 0 m; satellite imagery from Google Earth Pro, 2019) aligned with **b)** reference photographs of key fluvial features; leftmost photograph shows along-bank DAS cable during tap tests (full size photograph provided in Supplemental Figure S1). Solid yellow line indicates submerged DAS cable segment shown in panels c and d; dashed yellow line shows subaerial cable path (not used in this study). **c)** Example ~0.25 s of recorded in-creek DAS microstrain rate data. **d)** Total integrated signal power (P) and **e)** spatial spectrogram showing power spectral density (PSD) averaged over three 10 s segments of microstrain rate data at each position. Annotated regions I-III indicate banded spectral features visible below ~400 Hz in panel e. Vertical blue shaded bands indicate broadband signals colocated with turbulent streamflow features. Vertical dashed and dotted lines indicate locations of example spectra shown in Figure 3.

channel widths of 6.10, 10.06, and 14.33 m. Froude numbers calculated from measured flow velocities and depths for the rapids, riffle, and pools are 0.87, 0.38, and 0.11, respectively, indicating subcritical flow and consistent with previous studies documenting subcritical flow through pools and higher Froude numbers over rapids and gravel bars or riffles (e.g., MacVicar and Roy, 2007; Lumsdon et al., 2018). Throughout the deployment, the stream bed remained armored, and we visually observed no sediment transport.

### 3.3 DAS data processing and analysis

The Terra15 DAS system records optical phase-based deformation rate (equivalent to along-fiber velocity; Yang et al., 2022b). We converted deformation rate to along-cable microstrain rate ($\mu\varepsilon$/s or $10^{-6}$ $\varepsilon$/s) by finite differencing over a fixed fiber distance (commonly called "gauge length"; Parker et al., 2014) set to 3.24 m. The resulting microstrain rate (Figure 1c) is equivalent to the gradient in along-fiber velocity over 4 DAS channels.

We performed spectral analysis on 30 seconds of strain rate data along the submerged cable length. Flow characteristics were steady and did not vary over the entire duration of deployment, and we observed no notable differences across several 30 s segments during the acquisition period. We therefore averaged the amplitude spectra from three consecutive 10 s windows at each channel, then converted to power spectral density (PSD) by squaring and normalizing the average amplitude spectrum by the frequency bin width. We integrated the average PSD over all recorded frequencies (up to 10 kHz) to find the total acoustic power (P) (in $[\mu\varepsilon/s]^2$) at each point along the river (Figure 1d).

In Figure 1e, we present a spatial spectrogram or spatio-spectral map of the average PSD at each position along the submerged section of cable. These spatio-spectral data are shown over a limited frequency range up to 1 kHz to highlight key spectral features and offer a basis for comparison across the range of frequencies examined in previous studies. Spatial spectrograms are also provided on both linear and logarithmic axes up to 100 Hz in Supplemental Figure S2 and for the full range of observable frequencies up to 10 kHz in Supplemental Figure S3. To better enable visualization of the spectrum along-river, we also produced an animation of the spectrum up to 1 kHz paired with an auditory "soundscape" composed of spliced, consecutive 0.3 s segments of strain-rate sound files from each DAS channel along the creek (Supplemental Video 1 and Supplemental Figure S4). Full spectrograms (up to 10 kHz) for both the submerged and along-bank cable segments as well as the spectrum at any point along the channel can be explored in more detail via an interactive Matlab app (Roth et al., 2023).

Finally, we built a cross-correlation matrix representing along-stream signal similarity by calculating the cross-correlation between 30 s of strain rate data from each channel in the submerged section of cable with every other channel in the same section across a range of lag times. We use the highest correlation value between each pair of channels as a measure of the maximum cross-channel correlation (Figure 2).

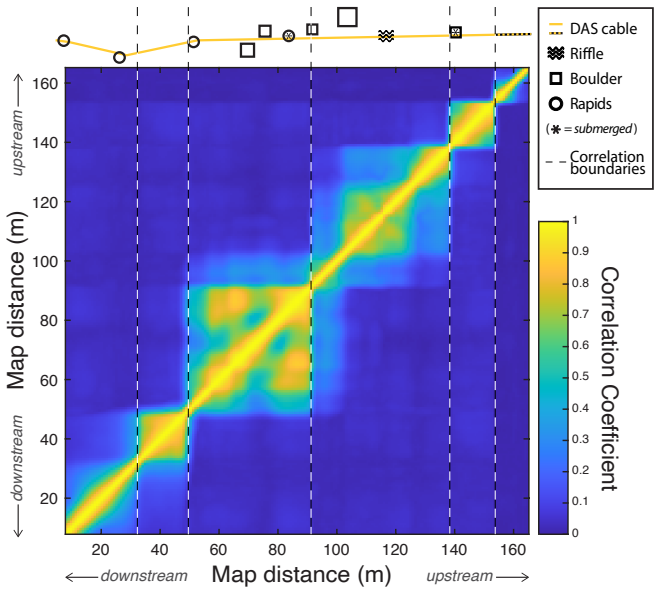


**Figure 2** Cross-correlation matrix representing maximum along-stream wave correlation between channel pairs in the submerged cable. Dashed lines show approximate locations of low-correlation boundaries between regions of high correlation.

## 4 Results

### 4.1 Spectral characteristics and correlation

Throughout the study reach, spectral power peaks between ~20 Hz and ~60 Hz (Supplemental Figure S2). We observe six regions with broadband signals (vertical blue shading centered at about ~8 m, 28 m, 53 m, 87 m, 117 m, and 141 m, Figure 1) colocated with the engineered rapids (three exposed and one submerged), a zone of shallow flow over the riffle (rightmost photo in Figure 1b), and a large, submerged boulder (Figure 1a). These broadband peaks are discernable across all resolved frequencies up to 10 kHz (Supplemental Figure S3, Supplemental Video 1, Roth et al., 2023) and correspond in space with peaks in total spectral power along the study reach (Figure 1d, and 1e).

The broadband peaks at the rapids and boulder correspond with zones of low along-stream wave correlation (Figure 2) that separate distinct regions of high correlation (i.e., each DAS channel is highly correlated with other channels inside its region and poorly correlated with channels outside of it). Starting at the upstream end (map distance ~165 m, Figure 2), the first high-correlation region corresponds with the part of the cable that was outside of the water. This section was excluded from Figure 1. The second correlated region starts where the cable enters the water and ends at the submerged boulder (Figure 1a). In the remaining regions, we see the highest correlation through the run-riffle reach and, farther downstream, the pools adjacent to each engineered rapid. A condensed version of Figures 1 and 2 is provided in the Supplement (Supplemental Figure S5) for easier spatial referencing between these results.

Rapids and, to a lesser extent, riffles are characterized by shallow, fast flows over rough beds, which promote shear, flow separation, eddy and wave formation, resulting in higher turbulence intensities than those observed in pools (Magirl et al., 2009; Wright and Kaplinski, 2011; McQuivey, 1973). At broader morphologic scales, riffle–pool or riffle-run sequences modulate turbulence, with riffles enhancing turbulent energy transfer while pools or runs act to dampen it (Marquis and Roy, 2011). Although measurements sufficient to quantify turbulence intensity or Reynolds numbers were not collected dur-

ing this experiment, visual observations of whitewater in the rapids and riffles and smoother flow in pools and runs support the inference that rapids and riffles host more turbulent flow conditions, whereas pools and runs are comparatively less turbulent. To better compare the spectral signatures associated with each of these morphologic features, we show example power spectral densities and their log-binned averages (Figure 3) from several broadband signals associated with flow inferred to be more turbulent, along with neighboring reaches with lower inferred turbulence (vertical dashed and dotted lines annotating Figure 1). Spectral power above ~4 kHz appears to be controlled by instrument response and is shown only in Supplemental Figure S6. All sites contain enhanced power with a flat spectrum at low frequencies and steeper spectral slopes beginning around ~50-65 Hz. The less turbulent examples from each pair of sites demonstrate slightly steeper spectral slopes at mid-frequencies and a more pronounced decline in spectral slopes at frequencies above ~500 Hz. Spectral flattening at high frequencies is particularly prominent in the upper pool and run shown in Figures 3c and 3d (dotted blue and purple lines in Figure 1c-e). The two farthest downstream rapids show broad spectral peaks over ~15–60 Hz (Figure 3a-b); spectra from the pools upstream of each rapid are similar in form but contain narrower peaks with maximum power at ~25–45 Hz and lower broadband power across the observed frequency range. The uppermost rapid and neighboring pool (Figure 3c) both demonstrate a similar, sharp peak at ~25–45 Hz, with the rapid again producing higher power across all frequencies; the pool additionally shows peaks at ~100 Hz and ~715 Hz. The spectrum at the riffle (Figure 3d) contains three distinct peaks at ~15 Hz, ~22 Hz, and ~30 Hz; all three peaks are also evident in the less turbulent run just upstream (Figure 3d), which has additional peaks at ~10 Hz, ~100 Hz, ~230 Hz, and ~340 Hz.

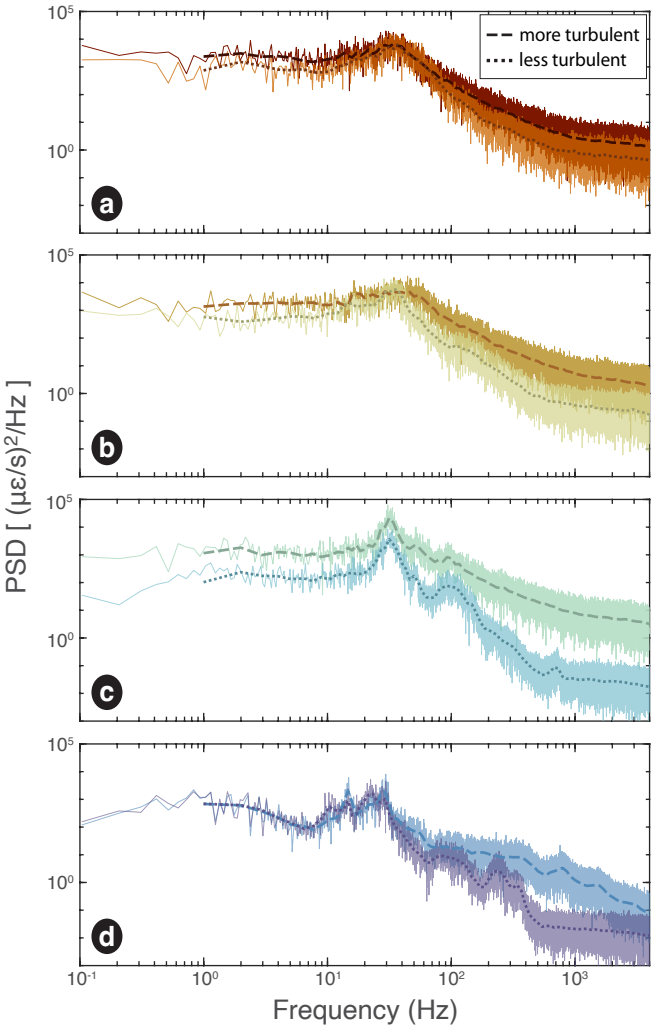


**Figure 3** Example power spectra comparing broadband signals (dashed lines) from regions with enhanced turbulence and neighboring regions (dotted lines) with less turbulent flow. Line colors correspond with Figure 1 and central lines show log-binned average power density for each spectrum. Starting at the downstream end of the study reach, spectra show a-c) the three rapids and pools immediately upstream of each rapid, and d) the run-riffle sequence upstream.

## 4.2 Knocking pulse signal

The broadband peak (Figure 1e) over the shallow riffle (map distance ~117 m) is also associated with a rapid "knocking" sound in the DAS soundscape (Supplemental Video 1, and Figure S4). This signal appears in the strain rate data as a series of quasiperiodic impulsive signals (dark blue dashed line at map distance ~117 m in Figure 1c) with linear moveout (i.e., a linear relationship observed between wave arrival time and distance) and recurrence intervals of ~0.05 – 0.09 s (Figure 1c). The apex or source location of these impulsive signals (location where each pulse is first recorded) is colocated with the broadband signal noted above (indicated by dashed blue line at map distance ~117 m on Figures 1c and 1e, respectively).

## 4.3 Banded spatio-spectral gliding

In the two largest correlated regions in Figure 2, the spatial spectrogram reveals a series of alternating spectral bands and bandgaps that shift or "glide" in frequency with position along the river (regions I–III in Figure 1e). In the pool above the uppermost rapid, the central frequencies of three visible bands increase with distance upstream (I, Figure 1e). The lowest band shifts from ~30 Hz just upstream of the rapids to ~90 Hz approximately 20 m upstream. We also observe at least eight bands increasing in frequency nearly symmetrically (II-III, Figure 1e) around the shallow riffle as flow deepens both upstream and downstream. Upstream of the riffle, where bands are more clearly resolved, the lowest frequency band increases from ~40 Hz to ~350 Hz within about 25 m of the central riffle. These bands and bandgaps are also visible in the example spectra for the uppermost pool (Figure 3c) and the riffle-run sequence (Figure 3d). See Supplement (Video 1 and Figure S4) or the interactive Matlab app (Roth et al., 2023) for visualizations of spatial evolution in DAS spectra along the study reach, in which the spectral gliding is particularly evident.

# 5 Discussion

Much like in-stream hydrophones, DAS systems can record acoustic waves transmitted through the water column and generated, for example, by either the flow or sediment particle collisions (Thorne, 2014). However, in addition to propagating through the water column, elastic waves can also propagate along the fiber optic DAS cable. Additionally, DAS data can capture interactions between the cable and its environment, such as impacts along the cable or shear stress exerted directly on the cable by the flow. Below, we explore the signals we observe in more detail, taking advantage of the array nature of DAS to investigate signal sources where possible and highlighting key similarities and differences with signals previously documented by hydrophone or seismic deployments.

## 5.1 Flow characteristics captured by DAS

Turbulence generates stochastic velocity fluctuations as eddies advect downstream, and is generally detected as broadband noise on hydrophones (e.g., Tonolla et al., 2009). The frequency range captured by our DAS data coincides with the expected rate of turbulent velocity fluctuations (~$10^{-1}$–$10^{4}$ Hz) associated with downstream advection of eddies in the inertial subrange, where turbulent energy is transferred from larger to progressively smaller eddy structures (Tennekes and Lumley, 1972). By Taylor's frozen turbulence hypothesis (Taylor, 1938), the period of velocity fluctuations at a given point represents the time for an eddy of a given size to advect past at the mean flow velocity $u$. The frequency of velocity fluctuations generated by eddies with characteristic length scale $L$ is therefore $f \sim \frac{u}{L}$. The maximum frequency of the inertial subrange, associated with the smallest turbulent length scale, i.e., the Kolmogorov microscale, is ~$10^{3}$–$10^{4}$ Hz for typical Reynolds numbers found in rivers (Tennekes and Lumley, 1972), and the minimum frequency varies with position within the water column. Far from the bed, the largest eddy size $L$ can be approximated as the flow depth $h$ or width $w$ (Jerolmack and Paola, 2010; Nikora, 2007), whereas eddies in the boundary layer at the bed are represented by the roughness-dependent turbulent mixing length (Schlichting, 1979) approximated as $L \sim 3\pi D_{50}$ (Gimbert et al., 2014), where $D_{50}$ is the median grain diameter. Using the range of measured flow velocities, corresponding flow depths, widths, and median grain size for Clear Creek, we estimate that turbulence in the inertial subrange produces power with minimum frequencies between ~0.02 and ~6 Hz throughout the study reach.

DAS should also detect signals from coherent flow structures (Nikora, 2007) arising from surface gravity waves and hydraulic or hydrodynamic disturbances (e.g., bed morphology-controlled pressure and velocity fluctuations; Marquis and Roy, 2010) that drive oscillations of the water surface (e.g., Nikora, 2007; Horoshenkov et al., 2013). These surface waves generate coherent pressure oscillations that couple into the water column as low-frequency signals, typically observed from < 1 Hz to ~10 Hz (e.g., Detert et al., 2010; Horoshenkov et al., 2013). Since the DAS cable is directly coupled to the flow and records frequencies in the ~$10^{-1}$–$10^{4}$ Hz range, it should therefore capture information about turbulent length scales and associated velocity fluctuations driven by both turbulent the energy cascade and coherent structures.

It is unclear to what extent the observed DAS signals also represent flow-generated strain propagating along the cable, which poses a significant challenge for interpreting DAS data in relation to local flow hydraulics (as discussed in Sections 5.2 and 5.3). Nonetheless, two lines of evidence suggest that our results retain interpretive value, as discussed below. First, cross-channel correlation (Figure 2) indicates minimal signal propagation across the boundaries between correlated regions, suggesting that signals recorded within any given correlated region are sourced from within the same region. Second, our observations are consistent with previous hydrophone and seismic measurements, which suggests that the DAS records are capturing genuine river-generated signals rather than artifacts, and therefore provide meaningful information about flow dynamics.

The signal decorrelation across rapids is consistent with expectations for both surface-wave–mediated signals and turbulent velocity fluctuations in the inertial subrange. The estimated Froude numbers for rapids (Fr = 0.87) approach the supercritical threshold (Fr > 1), whereas riffles (Fr = 0.38) and pools (Fr = 0.11) remain well within the subcritical regime. Even when depth-averaged Froude numbers indicate subcritical flow, as they do here, rapids often contain localized regions of supercritical flow (e.g., Magirl et al., 2009; Tinkler, 1997). As flows approach supercritical conditions, the upstream transmission of hydrodynamic disturbances via surface gravity waves and free-surface pressure or velocity fluctuations becomes increasingly restricted. Consequently, these surface-wave–mediated signals are less likely to transmit across rapids than across riffles or pools.

The highly correlated regions associated with pools and the uncorrelated boundaries and broadband spectral power we see near rapids and large boulders are also consistent with previous observations by hydrophones. Wave coherence (another measure of signal similarity) and well-defined frequency bands have been associated with more laminar flows (Chanaud and Powell, 1965; Howe, 1998; Matoza et al., 2010; Tonolla et al., 2011) or standing waves (Ronan et al., 2017), whereas incoherence and broadband noise are often found in more turbulent flows through rapids and riffles (e.g., Wysocki et al., 2007; Tonolla et al., 2010; Matoza et al., 2010). Broadband noise generation in turbulent flows is commonly ascribed to breaking waves in rapids (e.g., Lumsdon et al., 2018) and turbulence-induced bubble formation and collapse by cavitation, which can produce acoustic noise peaking between 0.01 and 1 kHz (Urick, 1983; Lurton, 2002). Turbulence-generated bubble plumes can also cause hydoacoustic incoherence due to scattering and absorption of background acoustic energy (Norton and Novarini, 2001).

Further, the dominant frequencies found in our DAS

data are broadly consistent with previous observations of flow-generated acoustic power recorded by in-stream hydrophones and seismometers. Several studies have found similar peak frequencies to those discussed in section 4.1 in comparable fluvial settings (Lugli and Fine, 2003; Wysocki et al., 2007; Tonolla et al., 2010; Nativ et al., 2025), though hydrophone data is often reported as sound pressure levels in discrete, low-resolution octave bands. Our spectra (Figure 3) also coarsely resemble lower resolution hydrophone observations (Tonolla et al., 2009, 2010, 2011) of root-mean-square acoustic sound pressure peaking in the tens of Hz and declining nonmonotonically through several hundred Hz. The observed increases in acoustic power in rapids and over the shallow riffle (where flow depths decrease and velocities increase) are also consistent with previous studies that have attributed variation in acoustic or seismic power up to the ~kHz range to flow hydraulics. Increases in seismic or acoustic power and frequency in rivers are often associated with increased flow velocity or relative roughness (the ratio of median grain size on the bed to flow depth) (e.g., Gimbert et al., 2014; Tonolla et al., 2010, 2011) and the presence of natural or artificial obstructions in the stream channel, including boulders (e.g., Osborne et al., 2022; Nativ et al., 2025) and hydrophone mounting infrastructure (e.g., Tonolla et al., 2009).

Although our study parameters do not permit a comprehensive investigation into the relationships between DAS spectral attributes and specific flow hydraulics, our findings suggest that this line of inquiry merits further consideration. Future work should prioritize improved precision in submerged DAS channel geolocation along with colocated measurements of flow velocity and turbulent velocity fluctuation time series using acoustic doppler velocimeters (ADVs) or electromagnetic current meters (ECMs). High frequency flow velocity time series measurements also allow direct comparison between DAS strain rate spectra and turbulent velocity spectra representing the distribution and dissipation of kinetic energy among different scales of turbulence (Tennekes and Lumley, 1972). In addition, these data can provide information on the frequency of vortex shedding (e.g., Aubrey and Trowbridge, 1985; Best, 1993; Kirkbride, 1993) and the flow structures and turbulent length scales associated with different bedforms (e.g., Nelson et al., 1993; Robert, 1997) and roughness (Robert et al., 1992; Clifford, 1996) to enable spatially explicit validation and interpretation of DAS strain rate data. For example, Wohl and Thompson (2000) note that flow acceleration and skin friction just upstream of steps (rapids) enhance near-bed turbulence, whereas form drag on large wakes and eddies immediately downstream leads to higher turbulence farther from the bed. DAS data recorded at different positions within the water column and validated with high quality ADV or ECM measurements could enable resolution of spatial variation in turbulent dynamics like these, or testing of more complex hypotheses.

Quantitative interpretation or prediction of DAS spectral characteristics relative to hydraulic variables will also require adaptation of theoretical models for acoustic signals generated by water turbulence, which currently focus explicitly on the signals recorded by bank-side seismometers (Gimbert et al., 2014).

## 5.2 Cable-bed interactions and wave propagation

The "knocking" sound detected at the shallow riffle (Supplemental Video 1), as well as the signal's impulsive forcing signature and broadband power spectrum (Figure 1c, 3b) are reminiscent of previously documented pulses generated by mobile sediment impacts (e.g., Geay et al., 2017). DAS records arrival times across many adjacent channels, enabling localization of impulsive sources and estimation of along-fiber wave speeds from the timing and moveout of first arrivals (Walter et al., 2020). To test the hypothesis that the "knocking" signals might originate from otherwise undetected sediment motion, we locate each source and infer propagation velocity based on the arrival times at each channel along the cable.

We manually identified 312 individual "knocking" impulse events in the waveform record for each DAS channel. We define a "knocking" event as a short-duration, impulsive, high-amplitude signal that produces clear first arrivals across neighboring DAS channels. Identification of event arrival times was semi-automated by cross-correlation of all traces with an analyst-selected reference trace. Earliest arrivals consistently occur at DAS channel 596 (Figure 4a), corresponding with a map distance of ~117 m (Figure 1).

We then used a grid search to optimize the wave propagation velocity and source-to-cable distance by minimizing the misfit between the observed and predicted arrival times. This allows us to determine whether the signal represents hydroacoustic waves propagating through the water or a disturbance propagating along the cable itself. Assuming propagation through a homogeneous medium, the predicted arrival time of a knocking signal at DAS channel $i$ is calculated as $t_i = t_0 + \frac{\sqrt{(x_i - x_0)^2 + z^2}}{v}$, where $t_0$ is the event origin time, $x_i$ is the along-cable position of the channel, $x_0$ is the along-cable position closest to the source (i.e., channel 596, the location of earliest arrivals), $z$ is the shortest distance from source to cable (i.e., orthogonal to the cable at position $x_0$), and $v$ is the homogeneous wave propagation velocity. We grid-searched over $z$ and $v$ values for each event to find the optimal values minimizing $\sqrt{\frac{1}{n}\sum (t_i - t_{i,obs})^2}$, or the root-mean-square misfits between calculated arrival times $t_i$ and observed arrival times $t_{i,obs}$, across all $n$ DAS channels with detectable first arrivals. Since the origin time ($t_0$) is not known, we treat it as a free parameter, removing the mean of the travel time misfit before calculating the RMS. In this way we are effectively fitting the relative arrival times at the different channels, rather than the absolute arrival times. Optimized wave propagation velocities were consistently around 2,100 m/s (Figures 4b-c), and optimized source-cable distances were bimodally distributed with peaks at 0 m and ~2 m (Figure 4d). We note, however, that because strain rate at each channel is averaged over

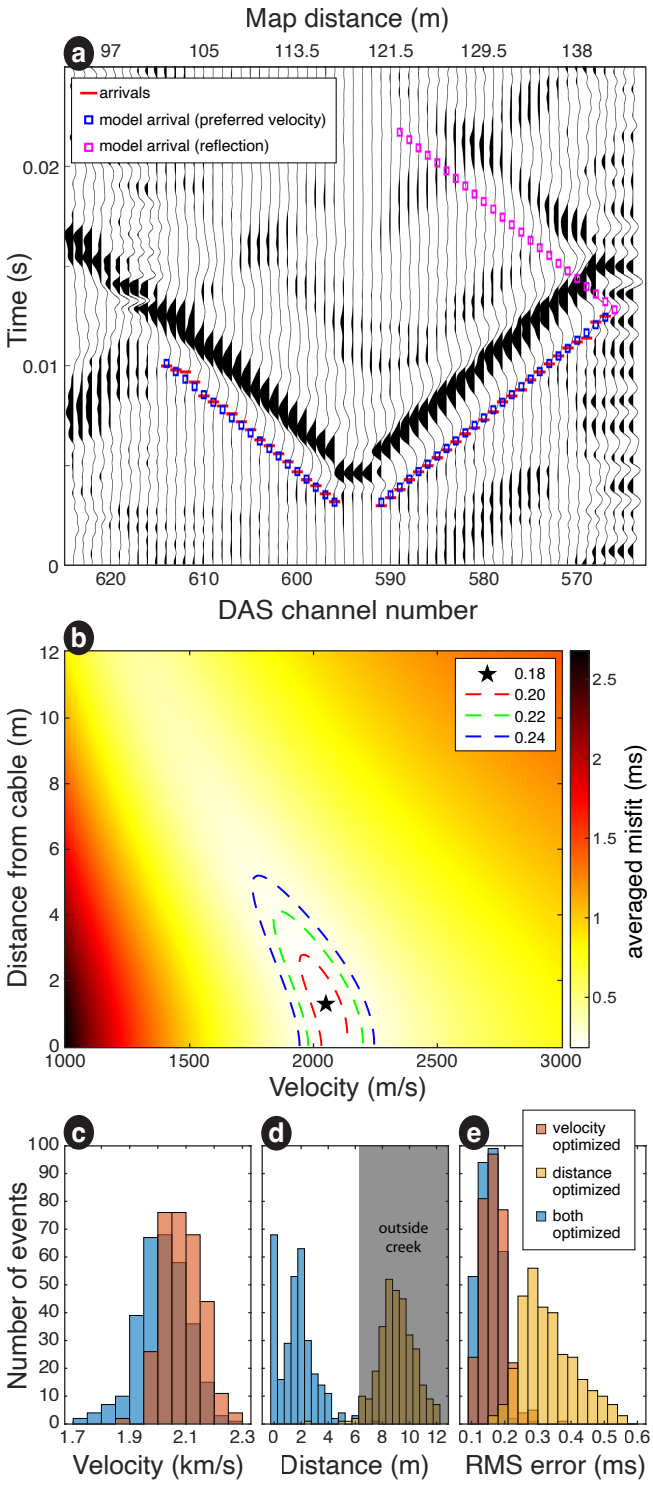


**Figure 4** a) Strain rate variable-area wiggle plot of waveforms from each DAS channel in a section of cable showing one "knocking" event with identified arrivals, calculated arrival times for the preferred propagation velocity, and calculated arrival times for a reflection. Note that the waveforms are consistent with an along-cable reflection occurring at the calculated times. Each trace is individually normalized by its maximum amplitude; black fill indicates positive strain rate amplitude. b) 2D grid of total model misfit as a joint function of optimized velocity and distance parameters. Star shows the minimum average misfit value of 0.1837, dashed lines show contours at misfits of 0.20, 0.22, and 0.24. c) Histogram of best-fitting propagation velocities v for all 312 "knocking" signals when the source distance from the cable z is set to zero or optimized. d) Best-fitting distance from the cable z when velocity v is set to 1450 m/s or optimized. Gray box indicates distances $\geq$6 m, which fall outside the creek. e) Misfit between observed and calculated travel times when both velocity v and distance from the cable z are optimized, when only velocity is optimized and distance from the cable is set to zero, and when distance away from the cable is optimized and the propagation velocity is set to 1450 m/s (the velocity of sound in water).

the surrounding 3.24 m (4 channels), the apparent travel time curves are rounded near the pulse apex $x_0$, which would tend to artificially increase the $z$ value found by the grid search. We intentionally neglect arrival times in the channels closest to $x_0$ to minimize this effect.

The optimal propagation velocities were well above the propagation velocity of sound in water (1,450 m/s) (blue bars, Figure 4c-e), suggesting propagation through a different medium, such as the cable itself. To explore this hypothesis, we conducted two more limited grid searches. In the first we assumed "knocks" originate from cable impacts on the bed and optimized velocity with the distance from the cable fixed to zero (red bars, Figure 4c,e). This produced similar optimal velocities (Figure 4c) and misfits (Figure 4e) relative to the unconstrained grid search. Second, we assumed an external source such as bedload sediment impacts and optimized only the distance away from the cable, setting the propagation velocity equal to that of sound in water (1,450 m/s) (yellow bars, Figure 4 c-e). This led to substantially higher misfits than in the previous two analyses (Figure 4e) and often distances away from the cable larger than the distance to the banks, both confirming that the "knocking" signal was not propagating through the water and indicating that its source was colocated with the cable itself.

Although the bed was observed to be armored with no evidence of sediment transport at the time of deployment, as a final precaution, we explore the theoretical probability that the "knocking" signal was generated by grain motion we were unable to observe visually. We used the river flow depths reported in Section 3.2 to estimate the riverbed shear stress and the associated potential for grain motion. The dimensionless Shields stress, $\tau$, a common metric for sediment mobility in rivers (Buffington and Montgomery, 1998) was estimated to fall between 10% and 65% of typical critical values required to initiate sediment movement (Supplemental Text S1), indicating that sediment movement was extremely unlikely.

Based on these results, we infer that the "knocking" signals were generated as turbulence-driven oscillations caused the cable to repeatedly impact the bed at the shallowest point along the gravel bar forming the riffle. This interpretation is further supported by the fact that we consistently observe what appears to be total reflection of the pulses at channel 569, around ~22 m upstream of the signal source (Figure 4a) at the location of a submerged boulder (Figure 1a, map distance of ~139 m). Along with the abrupt change in signal corre-

lation at this point (Figure 2), this observation suggests that the cable was snagged across the submerged boulder. We can conceive of no plausible mechanism for a wave propagating outside the cable to undergo the observed reflection.

We also observe occasional reflection of some "knocking" pulses downstream of the riffle (map distance ~85 m, Figure 1, Supplemental Figure S7), at the approximate location of the submerged rapid. Additionally, we occasionally find other impulse signals generated at both this location and farther downstream, where the cable enters the uppermost rapid (Supplemental Figure S7). In both of these locations, we infer that the cable may also have occasionally been dragged by the flow across a cement-reinforced boulder step. Combined, these observations suggest that, like the "knocking" signals observed over the riffle, cable interactions with the bed in other regions and some of the turbulent flow-generated signals from the rapids may occasionally propagate directly through the cable.

## 5.3 Spatio-spectral gliding from pulse train reflections

Because the impulses (Figure 1c, Supplemental Figure S7) are colocated with the instances of spatio-spectral gliding observed in the uppermost rapid and on either side of the riffle (Figure 1e, I-III), we hypothesized that these impulses may drive the gliding. To evaluate this possibility, we modeled the signals upstream of the riffle (Figure 1e, III), where knocking pulses are consistently reflected and gliding bands with associated bandgaps are most clearly expressed. At each DAS channel, the knocking signals and their reflections comprise a semi-regular series of lagged pulses (discrete, transient signals), also known as a pulse train or comb. Individual knocking signals at DAS channel 596 or map distance ~117 m (the apex of observed pulses and inferred source of cable impacts) were modeled as synthetic Ricker wavelets with amplitude $A$ at time $t$ given by

$$A(t) = \left(1 - 2\pi^2 f_r^2 t^2\right) e^{-\pi^2 f_r^2 t^2} \quad (1)$$

where peak frequency $f_r = 300Hz$ was determined based on the observed pulse width (~0.0067 s). We convolve the wavelet with a Dirac comb with variable pulse interval or lag time (0.068 ± random number between 0 and 0.02 s) to simulate pulse recurrence. We model the signal at each neighboring DAS channel accounting for wave propagation and reflection along the DAS cable by using the optimized wave speed (2100 m/s) and 1% amplitude decay per channel with 50% loss on reflection (Figure 4a, 5a ) based on the observed signal. Finally, we calculate the PSD generated by the time domain model pulse train at each DAS channel following the same procedure used to produce Figure 1e with our observational data. To isolate and compare the spectral features of interest, we detrend the observed and modeled spectra by subtracting sixth-order polynomial fits at each frequency (Figure 5b; raw observed and model spectrograms are shown in Supplemental Figure S8 for reference). Our model successfully reproduces the spectral bandgaps observed in the DAS data (Figure 5b-c, Supplemental Figure S8).

This phenomenon can be explained by the fact that the power spectrum of a pulse train depends on both the shape of the pulse waveform and the pulse repetition frequency along with its harmonics (e.g., Cox and Lewis, 1966; Zhang et al., 1992; Brillinger, 2011). A shift in the observed frequency bands therefore occurs when the pulse repetition frequency, or the lag times between knocking pulses and their reflections, shifts systematically in space as a function of the DAS channel distance from the reflection point. Downstream of the riffle and in the uppermost rapid (Figure 1e, I and II), the gliding harmonic bands are less distinct. We attribute this to higher variance in pulse lag times (Zhang et al., 1992) due to the inconsistent reflection or transmission of the knocking pulses (Figure 1e, I and II) as well as the turbulence-generated signals from the downstream rapid (Figure 1e, I) and other occasional impulses we observed in these regions (Supplemental Figure S7).

## 5.4 Hypothetical mechanisms for producing fluvial spatio-spectral gliding

Spatio-spectral gliding has not previously been documented in a river and, to our knowledge, has only been reported in a handful of cases in other environments (Cheng et al., 2021; Bouffaut et al., 2022; Rossi et al., 2022; Lior et al., 2022; Loureiro et al., 2025). Notably, all identified examples come from recent studies using DAS. The scarcity of examples may therefore reflect the fact that spatial spectrograms are not yet a common data visualization tool. The lack of well-established precedents makes interpretation of new observations challenging, but also underscores the value of drawing on cross-disciplinary examples. For example, Rossi et al. (2022) demonstrated that active source data from both a trenched DAS cable and a colocated geophone array exhibited nearly identical banded spatio-spectral gliding, arising when pulse signals separated in transit through layered substrates with different wavespeeds.

Motivated by the novelty of our observations and the rapid growth of DAS applications, we explore below several additional mechanisms that could plausibly generate spatio-spectral gliding or harmonics in fluvial settings. These include spatial variation in cable tension, lag times between bedload-generated pulses, and parameters controlling transport, hydraulics, and a range of elastic wave interference phenomena. Where relevant, we use our data and site characteristics to illustrate these mechanisms (quantitative examples provided in the Supplement), focusing on the upstream riffle-run reach (Figure 1e, III) where spectral features and stream morphology are best constrained. We also identify opportunities for future studies to test these hypotheses empirically.

### 5.4.1 Variable DAS cable tension

Resonance or standing waves within a DAS cable could, in principle, produce harmonic frequency bands with a spatial gradient in cable tension producing a spatial frequency shift. We can exclude this as a possible cause

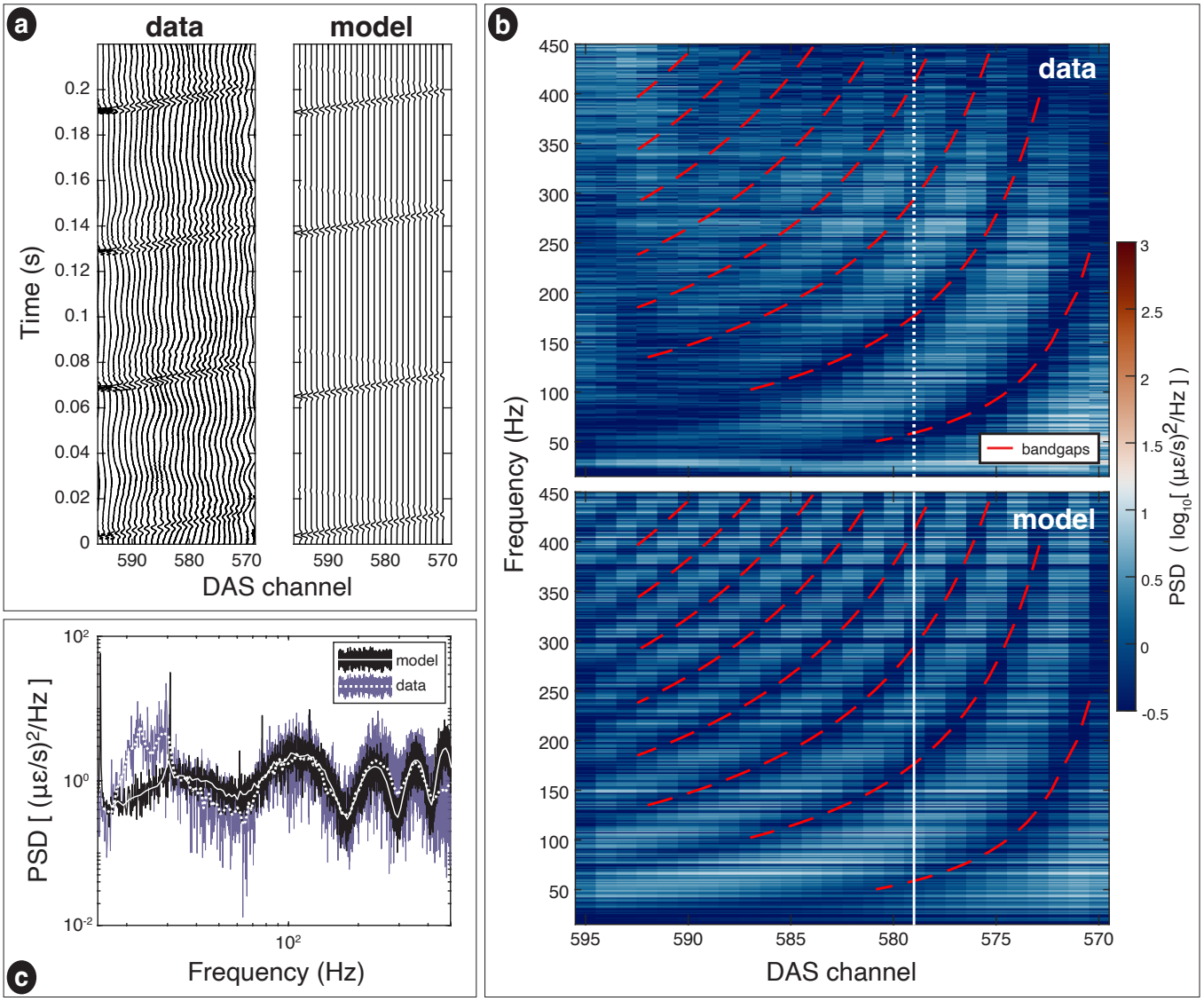


**Figure 5** a) Segments of "knocking" signals observed in the DAS data and synthetic pulses modeled as Ricker wavelets. b) Observed and modeled detrended spatial spectrograms of power spectral density (PSD) (shown on adjusted color scale relative to Fig. 1 to improve visibility), annotated with red dashed lines showing observed bandgaps traced from the DAS spectrogram. c) Example observed and modeled detrended power spectra and their log-binned averages (white lines) from DAS channel 579. Spectra detrended by best-fit sixth-order polynomials. Channel 579 is indicated by the white lines in part (b), and is the same channel shown in Fig. 3d.

of the spatial gliding observed here because the linear moveout of the "knocking" signal indicates constant wave propagation velocity in the cable. Since wave velocity in the DAS cable is a function of cable tension, we can infer uniform tension throughout this segment of cable. However, wave propagation speeds in DAS fiber under varying tension conditions have not yet been systematically studied, and robust constraints would benefit future applications with mobile or dynamically tensioned cables.

### 5.4.2 Bedload-generated recurring pulse signals

Bedload sediment transport could hypothetically generate acoustic harmonic bands with spatial gliding through mechanisms similar to those observed here. Sediment transport produces impulsive acoustic signals from grain-grain or grain-bed collisions (Johnson and Muir, 1969; Thorne, 2014; Geay et al., 2017; Krein et al., 2016). At sites where quasi-periodic impacts are spatially stable, such as recurring strikes of mobile grains against immobile clasts or the rocking of submobile cobbles, coherent harmonics could arise analogous to harmonic tremors from repeating pulses in volcanic and cryospheric systems (e.g., MacAyeal et al., 2008; Martin et al., 2010; Hotovec et al., 2013). Detection, however, may require ultra-sensitive DAS with submeter resolution since sediment-generated signals attenuate rapidly. Although most commercial DAS systems still operate at meter-scale resolutions to maintain signal-to-noise ratios (Dean et al., 2016), advances in fiber technology, interrogation and signal processing are pushing toward centimeter-scale systems (e.g., Aitkulov et al., 2022; Masoudi et al., 2022), opening new opportunities for studying fine-scale processes such as sediment transport.

### 5.4.3 Spatial variation in hydraulic or transport parameters

Spatio-spectral gliding in rivers could also arise from along-channel variation in hydraulic or transport parameters that control acoustic noise. This would be analogous to temporal-spectral gliding driven by time-varying conditions in terrestrial, volcanic, glacial, and submarine environments (e.g., Chouet, 1988; MacAyeal et al., 2008; Winberry et al., 2013; Heeszel et al., 2014). In fluvial settings, temporal-spectral gliding has been observed by only a handful of studies. Numerous studies have reported peak seismo-acoustic frequencies increasing with discharge or flow stage (Tonolla et al., 2010, 2011; Díaz et al., 2014; Dietze et al., 2019), consistent with the theoretical scaling between turbulent velocity fluctuations and mean flow velocity or discharge (Tennekes and Lumley, 1972). Such increases have also been attributed to the addition of high-frequency signals from bedload transport (e.g., Tonolla et al., 2011). Conversely, others have attributed anticorrelation between peak frequencies and discharge or stage to the progressive entrainment of larger particles (e.g., Díaz et al., 2014; Burtin et al., 2016) as particle size influences both impact-generated force pulse frequencies (e.g., McLaskey and Glaser, 2010) and hop lengths and rates during saltation (Sklar and Dietrich, 2004; Tsai et al., 2012). Anthony et al. (2018) also attributed a slight inverse scaling between discharge and peak horizontal-to-vertical ground acceleration frequencies to changes in shear wave velocity with progressive sediment saturation. Together, these findings suggest that spatio-spectral gliding could be diagnostic of spatial variation in flow hydraulics, streambed or channel morphology, or sediment sizes and transport rates. Such mechanisms could be responsible for unexplained observations of temporal-spectral gliding during flash flood-driven sediment transport events (Dietze et al., 2019) and following dam removal (Roth et al., 2011).

At our field site, however, hydraulic variation cannot explain the observed spatio-spectral gliding. Flow acceleration over the riffle should, in theory, shift turbulence-generated acoustic power toward higher frequencies. Instead, we observe a frequency decrease across the riffle (Figure 1e, III), inconsistent with a mean-flow mechanism. Although the DAS cable could have intersected a lower-velocity flow region near the frictional boundary at the bed, this mechanism would not generate the observed harmonics. This example highlights the importance of isolating the relative contributions of turbulence (or, similarly, sediment transport), direct fluid-cable shear, and cable-bed interactions in DAS data. Future progress will require adapting theoretical models for sediment- or turbulence-generated seismic signals (Tsai et al., 2012; Gimbert et al., 2014; Dietze et al., 2019; Nasr et al., 2022; Luong et al., 2024) to the acoustic and strain measurements made by submerged DAS cables. Such models would provide a physical framework to disentangle overlapping mechanisms, generate testable predictions, and guide controlled flume experiments designed to evaluate competing hypotheses.

### 5.4.4 Wave reflection, refraction and interference phenomena

Spatial gliding with harmonics could also hypothetically arise from wave reflection, refraction, and interference phenomena documented in other seismo-acoustic settings. For example, banded temporal-spectral gliding can result from resonance in opening or closing cracks in glaciers and volcanoes (Chouet, 1988; Heeszel et al., 2014) or shifting interference between direct and reflected waves (i.e., Lloyd's mirror; Lloyd, 1831) from moving sources such as aircraft, ships, landslides, and whales (Lo et al., 2002; Caplan-Auerbach et al., 2014; Audoly and Meyer, 2017; Pereira et al., 2020). Although such effects have been studied for decades in ocean acoustics (e.g., Hovem, 1993; Lurton, 2002), only recently has ocean-bottom DAS provided unequivocal evidence that they produce spatio-spectral gliding. Recent work with ocean-bottom DAS has revealed reflection- and scattering-based spatial variation in ambient noise spectra linked to shallow subsurface features (Cheng et al., 2021), and banded spatial gliding caused by Lloyd's mirror interference in whale calls reflected off the ocean surface (Bouffaut et al., 2022) or by interference in lateral and vertical earthquake-generated shear waves reflected off the edges of a submarine basin (Lior et al., 2022).

Whether similar processes operate in shallow, turbulent fluvial settings remains largely unexplored. Anthony et al. (2018) suggested that turbulence-generated Rayleigh and Love waves (Gimbert et al., 2014) could excite shear wave resonance in alluvial gravel layers, with resonant frequencies increasing as layers thin. This mechanism is physically plausible for our site (Supplemental Text S2), where the observed increase in peak frequencies both up- and downstream of the riffle (Figure 1b, III) coincide with bed morphology suggesting progressive thinning of alluvium. Building on prior work documenting self-sustained oscillations from shear flow over boundaries of varying geometries in laboratory experiments (Chanaud and Powell, 1965; Rockwell and Naudascher, 1979; Howe, 1998), volcanic gas jets (Matoza et al., 2010) and even asphalt or pavement surfaces (Ohiduzzaman et al., 2016), we also speculate that flow over alluvial beds could likewise excite harmonics or Helmholtz-type resonances in pore spaces between cobbles. This idea remains highly speculative and requires much deeper investigation, but if valid, spatio-spectral gliding like that observed here could serve as an indicator of strong and systematic spatial variability in pore space geometry (Supplemental Text S3). Reflection of acoustic waves or differential propagation through water, cable, and bed material could also in theory produce spatio-spectral gliding through a Lloyd's Mirror effect. However, our strain rate data show no secondary arrivals beyond those previously discussed, and the lag times between knocking pulses are too large for reflections to overlap. These mechanisms therefore appear unlikely to explain the banded gliding in our data.

Robust testing of all mechanisms will require detailed optimization modeling in fluvial settings with

well-mapped bed and subsurface structure and detailed characterization of bed materials. We recommend pairing DAS with dense, colocated instrumentation monitoring both water surface and bed surface elevations to constrain signal sources and resonant or reflective features.

## 5.5 Submerged cable deployment strategies

The cable-bed interactions identified in this study underscore the need for future research to develop deployment strategies minimizing cable-generated noise and assessing the implications of this noise for the interpretation of DAS data. Best practices for anchoring a DAS cable in a submerged stream setting have not been explored to date. Below, we propose several alternate deployment strategies and discuss potential challenges and opportunities associated with each approach.

### 5.5.1 Buried cable deployments

In alluvial rivers devoid of exposed bedrock or engineered cement reaches, cable burial within the bed offers a promising method to reduce cable motion as observed in our study. However, it is important to recognize that movement of bed material could still induce cable migration over individual flood events or seasonal timescales. Notably, deploying a DAS cable beneath the bed surface would effectively decouple it from direct fluid shear stresses generated by turbulent flow dynamics. Acoustic signals generated by flow or transport mechanisms would also be subject to high-frequency attenuation within the bed substrate, limiting the potential for validating DAS data by comparison with colocated hydrophone observations. Furthermore, large cobbles and pore spaces near the surface of a natural stream bed are anticipated to introduce significant heterogeneity in both cable coupling and near-field acoustic noise arising, for example, from pressure fluctuations transmitted by individual cobbles or hyporheic flow within the bed (Tonina and Buffington, 2009). Additionally, sediment erosion or deposition could lead to variability in depth-dependent temperature and pressure as sections of cable become exhumed or buried more deeply over time. Trenched streambed cable deployments may therefore prove suboptimal for explicit measurement of detailed streamflow hydraulics, but could provide a novel avenue for monitoring processes within the bed and hyporheic zone. Prior research has already demonstrated the utility of related distributed fiber optic sensing (DFOS) methods in similar contexts. For example, distributed temperature sensing (DTS) has proven effective in investigating deposition-induced temperature anomalies (e.g., Sebok et al., 2015) and surface water-groundwater interactions (e.g., Banks et al., 2022) in rivers, while and distributed strain sensing (DSS) can detect slow deformation in levees and embankments (e.g., Schenato, 2017). Future deployments could leverage integrated DFOS systems to enable simultaneous monitoring of vibration via DAS, temperature via DTS, and strain via DSS—thereby reducing unknown parameters and uncertainties inherent to natural stream settings.

### 5.5.2 Bed-surface deployments

Strategies should also be explored for cable deployment directly at the bed surface to enable direct measurement of shear stress fluctuations at the fluid interface. This undertaking is likely to be more straightforward in bedrock rivers, where cables can be affixed directly to the channel bed using industrial underwater adhesives. In contrast, alluvial river beds consisting of unconsolidated and potentially mobile sediment present a greater technical challenge. Our observations suggest that anchoring a DAS cable at intervals along a bed surface would generate significant noise due to resonances in the cable and interactions with the bed and anchors. We therefore recommend approaches focused on minimizing cable motion.

One such promising approach could involve deploying a cable attached to a rigid pipe or conduit analogous to Japanese pipe hydrophones, which have been successfully used in various fluvial environments (Mizuyama et al., 2010a,b; Goto et al., 2014). A rigid pipe or conduit could improve cable stationarity and would additionally enable the use of helically wound cables with broadside sensitivity to dynamic strain in multiple directions (e.g., Hornman, 2016). Other relatively well-supported approaches include utilizing heavy, motion-resistant cables like those used for ocean-bottom installations or securing a DAS cable to weighted materials secured along the riverbed. For example, a fire-hose assembly developed by Pandey et al. (2023) was shown to improve cable-ground coupling and isolate the cable from environmental noise in mobile terrestrial deployments. These designs represent promising directions for fluvial adaptation. We particularly emphasize the value of development and testing under controlled conditions in flume laboratories, where the limiting conditions for cable stability and coupling can be rigorously assessed.

Accurate monitoring of near-bed flow and transport conditions will also require careful attention to the hydrodynamic impacts of mounting or anchoring infrastructure. Self-generated wake turbulence is a known source of noise in hydrophone deployments, and could similarly challenge the systems proposed here despite their more streamlined footprints. Moreover, large, motion-resistant cables or pipe and conduit structures may be susceptible to wake-induced scour, leading to non-representative sediment transport measurements and inconsistent coupling with the bed surface. These risks highlight the importance of designing bed-surface deployments to minimize their footprint and avoid exceeding the natural roughness of the study reach, for example, by employing streamlined cables and mounting elements with diameters comparable to or smaller than the median grain size ($D_{50}$) of the bed surface.

Any rigid mounting structure would also require site response characterization, possibly on a recurring basis during long-term deployments to account for scour-induced variation in cable coupling or position, material degradation, or damage from abrasion and bedload impacts. This anticipated requirement is analogous to the repeated site-specific calibration needed for

hydrophone data to account for local acoustic variations. By contrast, DAS deployments offer the advantage of dense, spatially-distributed measurements that may enable correction for site-specific effects through post-processing and array-based analysis, thereby reducing the need for repeated calibration. While this distinction highlights a potential advantage of DAS technology, the effectiveness of such correction in turbulent, near-bed environments remains to be demonstrated.

### 5.5.3 Floating deployments

Finally, although our free-floating cable encountered notable challenges, future endeavors may surmount these by developing techniques for deploying floating DAS arrays capable of detecting turbulent fluctuations within the water column itself. For example, the use of newly developed "shape sensing" cables containing multiple cores capable of resolving dynamic cable curvature and torsion (e.g., Escobar-Vera et al., 2024) could potentially account for cable motion within a turbulent flow.

A free-floating cable is likely to generate some amount of noise due to wake; however, future research should evaluate wake noise relative to, for example, the self-generated turbulent noise that poses a similar challenge in hydrophone deployments (e.g., Belleudy et al., 2010). Advances in fields utilizing floating nodes (Jatoi et al., 2022) or freely hanging DAS cables (e.g., Martuganova et al., 2021) for applications in borehole geophysics or ocean acoustics will help enable better strategies for floating DAS deployments in rivers as well.

## 6 Conclusions and outlook

This study provides the first demonstration of high-resolution DAS data as a tool for fluvial monitoring. We map DAS spectral power and along-stream wave correlation to stream morphology and flow hydraulics, and find that decorrelated broadband power is associated with rapids and riffles, whereas highly correlated power in discrete frequency bands occurs in pools and runs. These findings are consistent with previous observations from in-stream hydrophones and bankside seismometers, and indicate that DAS captures information on along-stream variation in flow velocity or relative roughness.

We use array-based methods to investigate a quasi-periodic "knocking" pulse signal and infer that it was generated by cable-bed impacts and transmitted along the cable. A spatial spectrogram also reveals spatio-spectral gliding of discrete frequency bands in this location. A modelling exercise indicates that this phenomenon most likely results from the systematic along-cable variation in lag times between the "knocking" pulses and their reflections. This signal provides a convenient analog for demonstrating the ability of DAS arrays to locate unidentified sources such as the pulse signals commonly generated by bedload sediment transport (e.g., Johnson and Muir, 1969; Thorne, 2014; Geay et al., 2017; Krein et al., 2016). We further speculate that a wider range of processes could produce spatial and temporal frequency gliding in rivers, including the recurring pulse signals generated by sediment transport and acoustic wave reflection, refraction, and interference phenomena commonly observed in ocean acoustics (Lurton, 2002). Our observations emphasize the need for careful interpretation of spectral features in future deployments. They also underscore the capability of DAS data to meet this need by employing array techniques to effectively resolve signal sources and locations. Investigation of novel phenomena and quantitative interpretation of DAS data in terms of hydraulic or transport parameters will require development or adaptation of existing seismic models for water turbulence and bedload signals.

Best practices for submerged cable deployment are needed to address the unique challenges in DAS fluvial installations. Controlled flume experiments paired with modeling in computational fluid dynamics could characterize the behavior of submerged DAS cables under tension or fluid shear and assess cable-flow feedbacks. Similarly, resonances, reflections, or attenuation caused by cable burial could also be explored through flume experiments and elastic wave modeling. Co-deployment of hydrophones with DAS cables or multiple runs of submerged fiber could also provide a method to distinguish signals propagating within the flow from those traveling along the cable itself.

Incorporation of DAS in multi-instrument deployments could also enable valuable characterization of site- and process-specific effects on signal generation, modification, and attenuation in data from individual seismometers, geophones and hydrophones (e.g., Bakker et al., 2020; Lagarde et al., 2021; Osborne et al., 2022). The unsurpassed spatial coverage and resolution of DAS arrays, combined with the convenience of cable deployment and synchronized, centrally managed data logging, offers a technically and logistically feasible opportunity to link signal characteristics to source processes and facilitate model validation. These goals will be facilitated by ongoing progress in the development of new DAS systems with enhanced sensitivity, spatial resolution, and advanced capabilities such as torsion sensing.

## Acknowledgments

The authors thank Ron Nativ and one anonymous reviewer for comments and suggestions to improve this manuscript, and Emily Brodsky, Tieyuan Zhu, Rolf Hut, John Selker, Andy Wickert, Nic Brummel, Rick Aster, and Lori Tunstall for helpful advice and discussion. Hayden Jacobson assisted with field measurements and photography.

## 7 Data and code availability

Map services and data used in this study are available from the U.S. Geological Survey, National Geospatial Program. Stream discharge data were downloaded from USGS stream gage 06719505 (U.S. Geological Survey, 2016), and USGS 3DEP lidar data (U.S. Geological

Survey, 2015) were downloaded from OpenTopography (https://www.opentopography.org/). All data and Matlab scripts associated with this manuscript and used to produce figures, as well as an interactive Matlab application for closer examination of DAS spectra are published on Zenodo under a GNU General Public License at https://doi.org/10.5281/zenodo.7535671 (Roth et al., 2023). Figures 1 and 5 use Crameri perceptually uniform scientific colormaps (Crameri, 2018, 2023) produced by the crameri Matlab function (version 1.08) written by Chad A. Greene and available on GitHub at https://github.com/chadagreene/crameri. This work was initiated through participation in the NSF-funded DAS Research Coordination Network (RCN) (award EAR-1948737); additional resources and scripts for working with DAS data can be found at https://www.iris.edu/hq/initiatives/das_rcn.

## 8 Competing interests

The authors have no competing interests.

## References


Aitkulov, A., Marcon, L., Chiuso, A., Palmieri, L., and Galtarossa, A. Machine Learning Estimation of the Phase at the Fading Points of an OFDR-Based Distributed Sensor. *Sensors*, 23(1):262, Dec. 2022. doi: 10.3390/s23010262.

Ajo-Franklin, J. B., Dou, S., Lindsey, N. J., Monga, I., Tracy, C., Robertson, M., Rodriguez Tribaldos, V., Ulrich, C., Freifeld, B., Daley, T., and Li, X. Distributed Acoustic Sensing Using Dark Fiber for Near-Surface Characterization and Broadband Seismic Event Detection. *Scientific Reports*, 9(1), Feb. 2019. doi: 10.1038/s41598-018-36675-8.

Anthony, R. E., Aster, R. C., Ryan, S., Rathburn, S., and Baker, M. G. Measuring Mountain River Discharge Using Seismographs Emplaced Within the Hyporheic Zone. *Journal of Geophysical Research: Earth Surface*, 123(2):210–228, Feb. 2018. doi: 10.1002/2017jf004295.

Aubrey, D. G. and Trowbridge, J. H. Kinematic and dynamic estimates from electromagnetic current meter data. *Journal of Geophysical Research: Oceans*, 90(C5):9137–9146, Sept. 1985. doi: 10.1029/jc090ic05p09137.

Audoly, C. and Meyer, V. Measurement of radiated noise from surface ships-influence of the sea surface reflection coefficient on the Lloyd's mirror effect. In *Proceedings of ACOUSTICS 2017*, Perth, Australia, 2017.

Bakker, M., Gimbert, F., Geay, T., Misset, C., Zanker, S., and Recking, A. Field Application and Validation of a Seismic Bedload Transport Model. *Journal of Geophysical Research: Earth Surface*, 125 (5), May 2020. doi: 10.1029/2019jf005416.

Banks, E. W., Morgan, L. K., Sai Louie, A. J., Dempsey, D., and Wilson, S. R. Active distributed temperature sensing to assess surface water–groundwater interaction and river loss in braided river systems. *Journal of Hydrology*, 615:128667, Dec. 2022. doi: 10.1016/j.jhydrol.2022.128667.

Becker, M. W., Coleman, T. I., and Ciervo, C. C. Distributed Acoustic Sensing as a Distributed Hydraulic Sensor in Fractured Bedrock. *Water Resources Research*, 56(9), Aug. 2020. doi: 10.1029/2020wr028140.

Belleudy, P., Valette, A., and Graff, B. Passive hydrophone monitoring of bedload in river beds: first trials of signal spectral analyses. *USGS, Scientific Investigations Report*, 5091:67–84, 2010.

Best, J. On the interactions between turbulent flow structure, sediment transport and bedform development: some considerations from recent experimental research. In Clifford, N., R., J., and Hardisty, J., editors, *Turbulence: Perspectives on flow and sediment transfer*, page 61–92. John Wiley Sons, Ltd, 1993.

Booth, A. D., Christoffersen, P., Schoonman, C., Clarke, A., Hubbard, B., Law, R., Doyle, S. H., Chudley, T. R., and Chalari, A. Distributed Acoustic Sensing of Seismic Properties in a Borehole Drilled on a Fast-Flowing Greenlandic Outlet Glacier. *Geophysical Research Letters*, 47(13), July 2020. doi: 10.1029/2020gl088148.

Bouffaut, L., Taweesintananon, K., Kriesell, H. J., Rørstadbotnen, R. A., Potter, J. R., Landrø, M., Johansen, S. E., Brenne, J. K., Haukanes, A., Schjelderup, O., and Storvik, F. Eavesdropping at the Speed of Light: Distributed Acoustic Sensing of Baleen Whales in the Arctic. *Frontiers in Marine Science*, 9, July 2022. doi: 10.3389/fmars.2022.901348.

Brillinger, D. R. *The Spectral Analysis of Stationary Interval Functions*, page 25–55. Springer New York, Nov. 2011. doi: 10.1007/978-1-4614-1344-8_4.

Burtin, A., Hovius, N., and Turowski, J. M. Seismic monitoring of torrential and fluvial processes. *Earth Surface Dynamics*, 4(2): 285–307, Apr. 2016. doi: 10.5194/esurf-4-285-2016.

Caplan-Auerbach, J., Dziak, R. P., Bohnenstiehl, D. R., Chadwick, W. W., and Lau, T. Hydroacoustic investigation of submarine landslides at West Mata volcano, Lau Basin. *Geophysical Research Letters*, 41(16):5927–5934, Aug. 2014. doi: 10.1002/2014gl060964.

Chanaud, R. C. and Powell, A. Some Experiments concerning the Hole and Ring Tone. *The Journal of the Acoustical Society of America*, 37(5):902–911, May 1965. doi: 10.1121/1.1909476.

Chao, W.-A., Wu, Y.-M., Zhao, L., Tsai, V. C., and Chen, C.-H. Seismologically determined bedload flux during the typhoon season. *Scientific Reports*, 5(1), Feb. 2015. doi: 10.1038/srep08261.

Cheng, F., Chi, B., Lindsey, N. J., Dawe, T. C., and Ajo-Franklin, J. B. Utilizing distributed acoustic sensing and ocean bottom fiber optic cables for submarine structural characterization. *Scientific Reports*, 11(1), Mar. 2021. doi: 10.1038/s41598-021-84845-y.

Chouet, B. Resonance of a fluid-driven crack: Radiation properties and implications for the source of long-period events and harmonic tremor. *Journal of Geophysical Research: Solid Earth*, 93 (B5):4375–4400, May 1988. doi: 10.1029/jb093ib05p04375.

Clifford, N. Morphology and stage-dependent flow structure in a gravel-bed river. In Ashworth, P., Best, S., J.L., and McLelland, S., editors, *Coherent flow structures in open channels*, page 545–566. Wiley and Sons, Ltd, 1996.

Cook, K. L. and Dietze, M. Seismic Advances in Process Geomorphology. *Annual Review of Earth and Planetary Sciences*, 50 (1):183–204, May 2022. doi: 10.1146/annurev-earth-032320-085133.

Cook, K. L., Andermann, C., Gimbert, F., Adhikari, B. R., and Hovius, N. Glacial lake outburst floods as drivers of fluvial erosion in the Himalaya. *Science*, 362(6410):53–57, Oct. 2018. doi: 10.1126/science.aat4981.

Cox, D. R. and Lewis, P. A. W. *The Statistical Analysis of Series of Events*. Springer Netherlands, 1966. doi: 10.1007/978-94-011-7801-3.

Crameri, F. Geodynamic diagnostics, scientific visualisation and StagLab 3.0. *Geoscientific Model Development*, 11(6):2541–2562, June 2018. doi: 10.5194/gmd-11-2541-2018.

Crameri, F. Scientific colour maps, 2023. doi: 10.5281/ZENODO.1243862.

Dean, T., Cuny, T., and Hartog, A. H. The effect of gauge length on

axially incident P-waves measured using fibre optic distributed vibration sensing. *Geophysical Prospecting*, 65(1):184–193, July 2016. doi: 10.1111/1365-2478.12419.

Detert, M., Weitbrecht, V., and Jirka, G. H. Laboratory Measurements on Turbulent Pressure Fluctuations in and above Gravel Beds. *Journal of Hydraulic Engineering*, 136(10):779–789, Oct. 2010. doi: 10.1061/(asce)hy.1943-7900.0000251.

Dietze, M., Gimbert, F., Turowski, J., Stark, K., Cadol, D., and Laronne, J. The seismic view on sediment laden ephemeral flows–modelling of ground motion data for fluid and bedload dynamics in the Arroyo de los Piños. In *Sedhyd Conference 2019*, 2019.

Díaz, J., Ruíz, M., Crescentini, L., Amoruso, A., and Gallart, J. Seismic monitoring of an Alpine mountain river. *Journal of Geophysical Research: Solid Earth*, 119(4):3276–3289, Apr. 2014. doi: 10.1002/2014jb010955.

Escobar-Vera, C., Soriano-Amat, M., Martin-Lopez, S., Gonzalez-Herraez, M., and Fernández-Ruiz, M. R. Dynamic Curvature and Torsion Monitoring Using Quasi-Integer-Ratio Time-Expanded ΦOTDR. *Journal of Lightwave Technology*, 42(18):6522–6530, Sept. 2024. doi: 10.1109/jlt.2024.3445585.

Gao, K., Huang, L., Donahue, C., and Ajo-Franklin, J. *Monitoring urban hydrological environment monitoring using fiber optical sensing*. Oct. 2020. doi: 10.2172/1673329.

Geay, T., Belleudy, P., Gervaise, C., Habersack, H., Aigner, J., Kreisler, A., Seitz, H., and Laronne, J. B. Passive acoustic monitoring of bed load discharge in a large gravel bed river. *Journal of Geophysical Research: Earth Surface*, 122(2):528–545, Feb. 2017. doi: 10.1002/2016jf004112.

Geay, T., Michel, L., Zanker, S., and Rigby, J. R. Acoustic wave propagation in rivers: an experimental study. *Earth Surface Dynamics*, 7(2):537–548, June 2019. doi: 10.5194/esurf-7-537-2019.

Geay, T., Zanker, S., Misset, C., and Recking, A. Passive Acoustic Measurement of Bedload Transport: Toward a Global Calibration Curve? *Journal of Geophysical Research: Earth Surface*, 125 (8), Aug. 2020. doi: 10.1029/2019jf005242.

Gimbert, F., Tsai, V. C., and Lamb, M. P. A physical model for seismic noise generation by turbulent flow in rivers. *Journal of Geophysical Research: Earth Surface*, 119(10):2209–2238, Oct. 2014. doi: 10.1002/2014jf003201.

Goodling, P. J., Lekic, V., and Prestegaard, K. Seismic signature of turbulence during the 2017 Oroville Dam spillway erosion crisis. *Earth Surface Dynamics*, 6(2):351–367, May 2018. doi: 10.5194/esurf-6-351-2018.

Goto, K., Itoh, T., Nagayama, T., Kasai, M., and Marutani, T. Experimental and theoretical tools for estimating bedload transport using a Japanese pipe hydrophone. *International Journal of Erosion Control Engineering*, 7(4):101–110, 2014. doi: 10.13101/ijece.7.101.

Heeszel, D. S., Walter, F., and Kilb, D. L. Humming glaciers. *Geology*, 42(12):1099–1102, Dec. 2014. doi: 10.1130/g35994.1.

Hornman, J. Field trial of seismic recording using distributed acoustic sensing with broadside sensitive fibre-optic cables. *Geophysical Prospecting*, 65(1):35–46, Jan. 2016. doi: 10.1111/1365-2478.12358.

Horoshenkov, K. V., Nichols, A., Tait, S. J., and Maximov, G. A. The pattern of surface waves in a shallow free surface flow. *Journal of Geophysical Research: Earth Surface*, 118(3):1864–1876, Sept. 2013. doi: 10.1002/jgrf.20117.

Hotovec, A. J., Prejean, S. G., Vidale, J. E., and Gomberg, J. Strongly gliding harmonic tremor during the 2009 eruption of Redoubt Volcano. *Journal of Volcanology and Geothermal Research*, 259: 89–99, June 2013. doi: 10.1016/j.jvolgeores.2012.01.001.

Hovem, J. M. *Mechanisms of Bottom Loss in Underwater Acoustics*, page 21–40. Springer Netherlands, 1993. doi: 10.1007/978-94-011-1604-6_2.

Howe, M. S. *Acoustics of Fluid-Structure Interactions*. Cambridge University Press, Aug. 1998. doi: 10.1017/cbo9780511662898.

Jatoi, G. M., Das, B., Karim, S., Pabani, J. K., Krichen, M., Alroobaea, R., and Kumar, M. Floating Nodes Assisted Cluster-Based Routing for Efficient Data Collection in Underwater Acoustic Sensor Networks. *Computer Communications*, 195:137–147, Nov. 2022. doi: 10.1016/j.comcom.2022.08.014.

Jerolmack, D. J. and Daniels, K. E. Viewing Earth's surface as a soft-matter landscape. *Nature Reviews Physics*, 1(12):716–730, Oct. 2019. doi: 10.1038/s42254-019-0111-x.

Jerolmack, D. J. and Paola, C. Shredding of environmental signals by sediment transport. *Geophysical Research Letters*, 37 (19), Oct. 2010. doi: 10.1029/2010gl044638.

Johnson, P. and Muir, T. C. Acoustic Detection Of Sediment Movement. *Journal of Hydraulic Research*, 7(4):519–540, Jan. 1969. doi: 10.1080/00221686909500283.

Kirkbride, A. Observations of the influence of bed roughness on turbulence structure in depth limited flows over gravel beds. In French, N., R., J., and Hardisty, J., editors, *In Clifford*, page 185–196. John Wiley and Sons, Chichester, 1993.

Krein, A., Klinck, H., Eiden, M., Symader, W., Bierl, R., Hoffmann, L., and Pfister, L. Investigating the transport dynamics and the properties of bedload material with a hydro-acoustic measuring system. *Earth Surface Processes and Landforms*, 33(1):152–163, Aug. 2007. doi: 10.1002/esp.1576.

Krein, A., Schenkluhn, R., Kurtenbach, A., Bierl, R., and Barrière, J. Listen to the sound of moving sediment in a small gravel-bed river. *International Journal of Sediment Research*, 31(3): 271–278, Sept. 2016. doi: 10.1016/j.ijsrc.2016.04.003.

Lagarde, S., Dietze, M., Gimbert, F., Laronne, J. B., Turowski, J. M., and Halfi, E. Grain-Size Distribution and Propagation Effects on Seismic Signals Generated by Bedload Transport. *Water Resources Research*, 57(4), Apr. 2021. doi: 10.1029/2020wr028700.

Larose, E., Carrière, S., Voisin, C., Bottelin, P., Baillet, L., Guéguen, P., Walter, F., Jongmans, D., Guillier, B., Garambois, S., Gimbert, F., and Massey, C. Environmental seismology: What can we learn on earth surface processes with ambient noise? *Journal of Applied Geophysics*, 116:62–74, May 2015. doi: 10.1016/j.jappgeo.2015.02.001.

Lindsey, N. J. and Martin, E. R. Fiber-Optic Seismology. *Annual Review of Earth and Planetary Sciences*, 49(1):309–336, May 2021. doi: 10.1146/annurev-earth-072420-065213.

Lindsey, N. J., Dawe, T. C., and Ajo-Franklin, J. B. Illuminating seafloor faults and ocean dynamics with dark fiber distributed acoustic sensing. *Science*, 366(6469):1103–1107, 2019. doi: 10.1126/science.aay5881.

Lior, I., Mercerat, E. D., Rivet, D., Sladen, A., and Ampuero, J.-P. Imaging an Underwater Basin and Its Resonance Modes Using Optical Fiber Distributed Acoustic Sensing. *Seismological Research Letters*, 93(3):1573–1584, Apr. 2022. doi: 10.1785/0220210349.

Lloyd, H. On a New Case of Interference of the Rays of Light. *The Transactions of the Royal Irish Academy*, 17:171–177, 1831.

Lo, K., Perry, S., and Ferguson, B. Aircraft flight parameter estimation using acoustical Lloyd's mirror effect. *IEEE Transactions on Aerospace and Electronic Systems*, 38(1):137–151, 2002. doi: 10.1109/7.993235.

Loureiro, A., Schlaphorst, D., Matias, L., Pereira, A., Corela, C., Gonçalves, S., and Caldeira, R. First DAS observations from the GeoLab fibre in Madeira, Portugal. Feb. 2025. doi: 10.22541/es-

soar.173888335.59085596/v2.

Lugli, M. and Fine, M. L. Acoustic communication in two freshwater gobies: Ambient noise and short-range propagation in shallow streams. *The Journal of the Acoustical Society of America*, 114 (1):512–521, July 2003. doi: 10.1121/1.1577561.

Lumsdon, A. E., Artamonov, I., Bruno, M. C., Righetti, M., Tockner, K., Tonolla, D., and Zarfl, C. Soundpeaking - Hydropeaking induced changes in river soundscapes. *River Res. Appl.*, 34(1): 3–12, Jan. 2018. doi: 10.1002/rra.3229.

Luong, L., Cadol, D., Bilek, S., McLaughlin, J. M., Laronne, J. B., and Turowski, J. M. Seismic Modeling of Bedload Transport in a Gravel-Bed Alluvial Channel. *Journal of Geophysical Research: Earth Surface*, 129(9), Sept. 2024. doi: 10.1029/2024jf007761.

Lurton, X. *An introduction to underwater acoustics: principles and applications*, volume 2. Springer, London, 2002.

MacAyeal, D. R., Okal, E. A., Aster, R. C., and Bassis, J. N. Seismic and hydroacoustic tremor generated by colliding icebergs. *Journal of Geophysical Research: Earth Surface*, 113(F3), Aug. 2008. doi: 10.1029/2008jf001005.

MacVicar, B. J. and Roy, A. G. Hydrodynamics of a forced riffle pool in a gravel bed river: 1. Mean velocity and turbulence intensity. *Water Resources Research*, 43(12), Dec. 2007. doi: 10.1029/2006wr005272.

Magirl, C. S., Gartner, J. W., Smart, G. M., and Webb, R. H. Water velocity and the nature of critical flow in large rapids on the Colorado River, Utah. *Water Resources Research*, 45(5), May 2009. doi: 10.1029/2009wr007731.

Malehmir, A., Socco, L., Bastani, M., Krawczyk, C., Pfaffhuber, A., Miller, R., Maurer, H., Frauenfelder, R., Suto, K., Bazin, S., and Merz, K. *Near-surface geophysical characterization of areas prone to natural hazards: a review of the current and perspective on the future*, page 51–146. Elsevier, 2016. doi: 10.1016/bs.agph.2016.08.001.

Marquis, G. A. and Roy, A. G. Bridging the gap between turbulence and larger scales of flow motions in rivers. *Earth Surface Processes and Landforms*, 36(4):563–568, Feb. 2011. doi: 10.1002/esp.2131.

Martin, S., Drucker, R., Aster, R., Davey, F., Okal, E., Scambos, T., and MacAyeal, D. Kinematic and seismic analysis of giant tabular iceberg breakup at Cape Adare, Antarctica. *Journal Geophysical Research: Solid Earth*, 115(B6), June 2010.

Martuganova, E., Stiller, M., Bauer, K., Henninges, J., and Krawczyk, C. M. Cable reverberations during wireline distributed acoustic sensing measurements: their nature and methods for elimination. *Geophysical Prospecting*, 69(5):1034–1054, May 2021. doi: 10.1111/1365-2478.13090.

Masoudi, A., Lee, T., Beresna, M., and Brambilla, G. 10-cm spatial resolution distributed acoustic sensor based on an ultra low-loss enhanced backscattering fiber. *Optics Continuum*, 1(9): 2002, Sept. 2022. doi: 10.1364/optcon.468673.

Matoza, R. S., Fee, D., and Garcés, M. A. Infrasonic tremor wavefield of the Pu'u 'Ō'ō crater complex and lava tube system, Hawaii, in April 2007. *Journal of Geophysical Research: Solid Earth*, 115 (B12), Dec. 2010. doi: 10.1029/2009jb007192.

McLaskey, G. C. and Glaser, S. D. Hertzian impact: experimental study of the force pulse and resulting stress waves. *The Journal of the Acoustical Society of America*, 128(3):1087–1096, Sept. 2010. doi: 10.1121/1.3466847.

McQuivey, R. S. *Summary of turbulence data from rivers, conveyance channels, and laboratory flumes*. 1973. doi: 10.3133/pp802b.

Michlmayr, G., Chalari, A., Clarke, A., and Or, D. Fiber-optic high-resolution acoustic emission (AE) monitoring of slope failure. *Landslides*, 14(3):1139–1146, Dec. 2016. doi: 10.1007/s10346-016-0776-5.

Misset, C., Recking, A., Legout, C., Bakker, M., Bodereau, N., Borgniet, L., Cassel, M., Geay, T., Gimbert, F., Navratil, O., Piegay, H., Valsangkar, N., Cazilhac, M., Poirel, A., and Zanker, S. Combining multi-physical measurements to quantify bedload transport and morphodynamics interactions in an Alpine braiding river reach. *Geomorphology*, 351:106877, Feb. 2020. doi: 10.1016/j.geomorph.2019.106877.

Mizuyama, T., Laronne, J., Nonaka, M., Sawada, T., Satofuka, Y., Matsuoka, M., Yamashita, S., Sako, Y., Tamaki, S., Watari, M., and Yamaguchi, S. Calibration of a passive acoustic bedload monitoring system in Japanese mountain rivers. *US Geological Survey Scientific Investigations Report*, 5091:296–318, 2010a.

Mizuyama, T., Oda, A., Laronne, J., Nonaka, M., and Matsuoka, M. Laboratory tests of a Japanese pipe geophone for continuous acoustic monitoring of coarse bedload. In *US Geological Survey Scientific Investigations Report*, volume 5091, page 319–335. 2010b.

Nasr, M., Geay, T., Zanker, S., and Recking, A. A Physical Model for Acoustic Noise Generated by Bedload Transport in Rivers. *Journal of Geophysical Research: Earth Surface*, 127(1), Jan. 2022. doi: 10.1029/2021jf006167.

Nativ, R., Turowski, J. M., Chang, J., Hovius, N., Yang, C., Chen, W., Chang, W., and Laronne, J. B. Stationary Boulders Increase River Seismic Frequency via Turbulence. *Geophysical Research Letters*, 52(6), Mar. 2025. doi: 10.1029/2024gl113784.

Nelson, J. M., McLean, S. R., and Wolfe, S. R. Mean flow and turbulence fields over two-dimensional bed forms. *Water Resources Research*, 29(12):3935–3953, Dec. 1993. doi: 10.1029/93wr01932.

Nikora, V. *3 Hydrodynamics of gravel-bed rivers: scale issues*, page 61–81. Elsevier, 2007. doi: 10.1016/s0928-2025(07)11113-5.

Norton, G. V. and Novarini, J. C. On the relative role of sea-surface roughness and bubble plumes in shallow-water propagation in the low-kilohertz region. *The Journal of the Acoustical Society of America*, 110(6):2946–2955, Dec. 2001. doi: 10.1121/1.1414883.

Ohiduzzaman, M., Sirin, O., Kassem, E., and Rochat, J. State-of-the-Art Review on Sustainable Design and Construction of Quieter Pavements—Part 1: Traffic Noise Measurement and Abatement Techniques. *Sustainability*, 8(8):742, Aug. 2016. doi: 10.3390/su8080742.

Osborne, W. A., Hodge, R. A., Love, G. D., Hawkin, P., and Hawkin, R. E. Babbling brook to thunderous torrent: Using sound to monitor river stage. *Earth Surface Processes and Landforms*, 46 (13):2656–2670, Sept. 2021. doi: 10.1002/esp.5199.

Osborne, W. A., Hodge, R. A., Love, G. D., Hawkin, P., and Hawkin, R. E. The Influence of In-Channel Obstacles on River Sound. *Water Resources Research*, 58(4), Apr. 2022. doi: 10.1029/2021wr031567.

Pandey, A., Shragge, J., Chambers, D., and Girard, A. J. Developing a distributed acoustic sensing seismic land streamer: Concept and validation. *Geophysics*, 88(6):WC59–WC67, Sept. 2023. doi: 10.1190/geo2023-0072.1.

Parker, T., Shatalin, S., and Farhadiroushan, M. Distributed Acoustic Sensing – a new tool for seismic applications. *First Break*, 32 (2), Feb. 2014. doi: 10.3997/1365-2397.2013034.

Pereira, A., Harris, D., Tyack, P., and Matias, L. On the use of the Lloyd's Mirror effect to infer the depth of vocalizing fin whales. *The Journal of the Acoustical Society of America*, 148(5): 3086–3101, Nov. 2020. doi: 10.1121/10.0002426.

Petrut, T., Geay, T., Gervaise, C., Belleudy, P., and Zanker, S. Passive acoustic measurement of bedload grain size distribution using

self-generated noise. *Hydrology and Earth System Sciences*, 22 (1):767–787, Jan. 2018. doi: 10.5194/hess-22-767-2018.

Piégay, H., Arnaud, F., Belletti, B., Bertrand, M., Bizzi, S., Carbonneau, P., Dufour, S., Liébault, F., Ruiz-Villanueva, V., and Slater, L. Remotely sensed rivers in the Anthropocene: state of the art and prospects. *Earth Surface Processes and Landforms*, 45(1): 157–188, Jan. 2020. doi: 10.1002/esp.4787.

Rickenmann, D. Bedload Transport Measurements with Geophones, Hydrophones, and Underwater Microphones (Passive Acoustic Methods), May 2017. doi: 10.1002/9781118971437.ch7.

Robert, A. Characteristics of velocity profiles along riffle-pool sequences and estimates of bed shear stress. *Geomorphology*, 19 (1–2):89–98, May 1997. doi: 10.1016/s0169-555x(96)00049-9.

Robert, A., Roy, A. G., and De Serres, B. Changes in velocity profiles at roughness transitions in coarse grained channels. *Sedimentology*, 39(5):725–735, Oct. 1992. doi: 10.1111/j.1365-3091.1992.tb02149.x.

Rockwell, D. and Naudascher, E. Self-sustained oscillations of impinging free shear layers. *Annu. Rev. Fluid Mech.*, 11(1):67–94, Jan. 1979. doi: 10.1146/annurev.fl.11.010179.000435.

Rodríguez Tribaldos, V. and Ajo-Franklin, J. B. Aquifer Monitoring Using Ambient Seismic Noise Recorded With Distributed Acoustic Sensing (DAS) Deployed on Dark Fiber. *Journal of Geophysical Research: Solid Earth*, 126(4), Mar. 2021. doi: 10.1029/2020jb021004.

Ronan, T. J., Lees, J. M., Mikesell, T. D., Anderson, J. F., and Johnson, J. B. Acoustic and Seismic Fields of Hydraulic Jumps at Varying Froude Numbers. *Geophysical Research Letters*, 44(19): 9734–9741, Oct. 2017. doi: 10.1002/2017gl074511.

Rossi, M., Wisén, R., Vignoli, G., and Coni, M. Assessment of Distributed Acoustic Sensing (DAS) performance for geotechnical applications. *Engineering Geology*, 306:106729, Sept. 2022. doi: 10.1016/j.enggeo.2022.106729.

Roth, D., Finnegan, N., Brodsky, E., and Stark, C. A collision-based model for measuring bedload transport from the seismic waves generated by rivers. In *AGU Fall Meeting Abstracts*, volume 2011, page 22 –05, 2011.

Roth, D. L., Brodsky, E. E., Finnegan, N. J., Rickenmann, D., Turowski, J. M., and Badoux, A. Bed load sediment transport inferred from seismic signals near a river. *Journal of Geophysical Research: Earth Surface*, 121(4):725–747, Apr. 2016. doi: 10.1002/2015jf003782.

Roth, D. L., Finnegan, N. J., Brodsky, E. E., Rickenmann, D., Turowski, J. M., Badoux, A., and Gimbert, F. Bed load transport and boundary roughness changes as competing causes of hysteresis in the relationship between river discharge and seismic amplitude recorded near a steep mountain stream. *Journal of Geophysical Research: Earth Surface*, 122(5):1182–1200, May 2017. doi: 10.1002/2016jf004062.

Roth, D. L., Bezada, M. J., Jin, G., and Titov, A. A river on fiber: spatially continuous fluvial monitoring with distributed acoustic sensing – Data, Matlab Scripts and App, 2023. doi: 10.5281/ZENODO.7535672.

Schenato, L. A Review of Distributed Fibre Optic Sensors for Geo-Hydrological Applications. *Applied Sciences*, 7(9):896, Sept. 2017. doi: 10.3390/app7090896.

Schmandt, B., Aster, R. C., Scherler, D., Tsai, V. C., and Karlstrom, K. Multiple fluvial processes detected by riverside seismic and infrasound monitoring of a controlled flood in the Grand Canyon. *Geophysical Research Letters*, 40(18):4858–4863, Sept. 2013. doi: 10.1002/grl.50953.

Schmandt, B., Gaeuman, D., Stewart, R., Hansen, S., Tsai, V., and Smith, J. Seismic array constraints on reach-scale bedload transport. *Geology*, 45(4):299–302, Apr. 2017. doi: 10.1130/g38639.1.

Sebok, E., Duque, C., Engesgaard, P., and Boegh, E. Application of Distributed Temperature Sensing for coupled mapping of sedimentation processes and spatio-temporal variability of groundwater discharge in soft-bedded streams. *Hydrological Processes*, 29(15):3408–3422, Mar. 2015. doi: 10.1002/hyp.10455.

Sklar, L. S. and Dietrich, W. E. A mechanistic model for river incision into bedrock by saltating bed load. *Water Resources Research*, 40(6), June 2004. doi: 10.1029/2003wr002496.

Taylor, G. I. The Spectrum of Turbulence. *Proceedings of the Royal Society of London. Series A - Mathematical and Physical Sciences*, 164(919):476–490, Feb. 1938. doi: 10.1098/rspa.1938.0032.

Tennekes, H. and Lumley, J. L. *A First Course in Turbulence*. The MIT Press, 1972. doi: 10.7551/mitpress/3014.001.0001.

Thorne, P. D. An overview of underwater sound generated by interparticle collisions and its application to the measurements of coarse sediment bedload transport. *Earth Surface Dynamics*, 2(2):531–543, Dec. 2014. doi: 10.5194/esurf-2-531-2014.

Thorne, P. D. and Hanes, D. M. A review of acoustic measurement of small-scale sediment processes. *Continental Shelf Research*, 22(4):603–632, Mar. 2002. doi: 10.1016/s0278-4343(01)00101-7.

Tinkler, K. Critical flow in rockbed streams with estimated values for Manning's n. *Geomorphology*, 20(1–2):147–164, Sept. 1997. doi: 10.1016/s0169-555x(97)00011-1.

Tonina, D. and Buffington, J. M. Hyporheic Exchange in Mountain Rivers I: Mechanics and Environmental Effects. *Geography Compass*, 3(3):1063–1086, May 2009. doi: 10.1111/j.1749-8198.2009.00226.x.

Tonolla, D., Lorang, M. S., Heutschi, K., and Tockner, K. A flume experiment to examine underwater sound generation by flowing water. *Aquatic Sciences*, 71(4):449–462, July 2009. doi: 10.1007/s00027-009-0111-5.

Tonolla, D., Acuña, V., Lorang, M. S., Heutschi, K., and Tockner, K. A field-based investigation to examine underwater soundscapes of five common river habitats. *Hydrological Processes*, 24(22): 3146–3156, May 2010. doi: 10.1002/hyp.7730.

Tonolla, D., Lorang, M. S., Heutschi, K., Gotschalk, C. C., and Tockner, K. Characterization of spatial heterogeneity in underwater soundscapes at the river segment scale. *Limnology and Oceanography*, 56(6):2319–2333, Nov. 2011. doi: 10.4319/lo.2011.56.6.2319.

Trimble, D. and Machette, M. *Geologic Map of the Greater Denver Area, Front Range Urban Corridor*. Geological Survey Geologic Investigations Series. U.S, Colorado, 2003.

Tsai, V. C., Minchew, B., Lamb, M. P., and Ampuero, J. A physical model for seismic noise generation from sediment transport in rivers. *Geophysical Research Letters*, 39(2), Jan. 2012. doi: 10.1029/2011gl050255.

Urick, R. *Principles of underwater sound*. McGraw-Hill, New York, 3rd edn edition, 1983.

U.S. Geological Survey. USGS 3D Elevation Program Lidar Point Cloud CO SoPlatteRiver Lot5 2013 LAS 2015. 2015. https://portal.opentopography.org/usgsDataset.jsp?dsid=USGS_LPC_CO_SoPlatteRiver_Lot5_2013_LAS_2015. accessed through OpenTopography at URL.

U.S. Geological Survey. National Water Information System data available on the World Wide Web (USGS Water Data for the Nation), 2016. https://waterdata.usgs.gov/nwis/inventory/?site_no=06719505&agency_cd=USGS.

Van Horn, R. Surficial and Bedrock Geologic Map of the Golden Quadrangle, 1972. https://pubs.usgs.gov/of/2001/of01-223/berquist.html. Geological Survey, Map I-761-A.

Walter, F., Gräff, D., Lindner, F., Paitz, P., Köpfli, M., Chmiel, M., and Fichtner, A. Distributed acoustic sensing of microseismic sources and wave propagation in glaciated terrain. *Nature Communications*, 11(1), May 2020. doi: 10.1038/s41467-020-15824-6.

Winberry, P. J., Anandakrishnan, S., Wiens, D. A., and Alley, R. B. Nucleation and seismic tremor associated with the glacial earthquakes of Whillans Ice Stream, Antarctica. *Geophysical Research Letters*, 40(2):312–315, Jan. 2013. doi: 10.1002/grl.50130.

Wohl, E. E. and Thompson, D. M. Velocity characteristics along a small step-pool channel. *Earth Surface Processes and Landforms*, 25(4):353–367, Apr. 2000. doi: 10.1002/(sici)1096-9837(200004)25:4<353::aid-esp59>3.0.co;2-5.

Wright, S. A. and Kaplinski, M. Flow structures and sandbar dynamics in a canyon river during a controlled flood, Colorado River, Arizona. *Journal of Geophysical Research: Earth Surface*, 116 (F1), Mar. 2011. doi: 10.1029/2009jf001442.

Wysocki, L. E., Amoser, S., and Ladich, F. Diversity in ambient noise in European freshwater habitats: Noise levels, spectral profiles, and impact on fishes. *The Journal of the Acoustical Society of America*, 121(5):2559–2566, May 2007. doi: 10.1121/1.2713661.

Wyss, C. R., Rickenmann, D., Fritschi, B., Turowski, J. M., Weitbrecht, V., Travaglini, E., Bardou, E., and Boes, R. M. Laboratory flume experiments with the S wiss plate geophone bed load monitoring system: 2. Application to field sites with direct bed load samples. *Water Resources Research*, 52(10):7760–7778, Oct. 2016. doi: 10.1002/2016wr019283.

Yang, J., Shragge, J., and Jin, G. Filtering Strategies for Deformation-Rate Distributed Acoustic Sensing. *Sensors*, 22 (22):8777, Nov. 2022. doi: 10.3390/s22228777.

Zhang, Y.-T., Frank, C., Rangayyan, R., and Bell, G. Mathematical modeling and spectrum analysis of the physiological patello-femoral pulse train produced by slow knee movement. *IEEE Transactions on Biomedical Engineering*, 39(9):971–979, 1992. doi: 10.1109/10.256431.